

Article

Seismo-VLAB: An Open-Source Software for Soil–Structure Interaction Analyses

Danilo S. Kusanovic ^{1,*}, Elnaz E. Seylabi ², Peyman Ayoubi ³, Kien T. Nguyen ⁴, Joaquin Garcia-Suarez ⁵, Albert R. Kottke ⁶ and Domniki Asimaki ³

¹ Departamento de Obras Civiles, Universidad Técnica Federico Santa María, Valparaíso 2340000, Chile

² Department of Civil and Environmental Engineering, University of Nevada, Reno, NV 89557, USA

³ Department of Mechanical and Civil Engineering, California Institute of Technology, Pasadena, CA 91125, USA

⁴ Faculty of Civil Engineering, Ho Chi Minh City University of Technology, Ho Chi Minh City 70000, Vietnam; nguyentrungkien@hcmut.edu.vn

⁵ Institute of Civil Engineering, Institute of Materials École Polytechnique Fédérale de Lausanne, 1015 Lausanne, Switzerland

⁶ Pacific Gas & Electric, San Francisco, CA 94612, USA

* Correspondence: danilo.kusanovic@usm.cl

Abstract: In the fields of structural and geotechnical engineering, improving the understanding of soil–structure interaction (SSI) effects is critical for earthquake-resistant design. Engineers and practitioners often resort to finite element (FE) software to advance this objective. Unfortunately, the availability of software equipped with boundary representation for absorbing scattered waves and ensuring consistent input ground motion prescriptions, which is necessary for accurately representing SSI effects, is currently limited. To address such limitations, the authors developed *Seismo-VLAB* (SVL v1.0-stable) an open-source software designed to perform SSI simulations. The methodology considers the integration of advanced techniques, including the domain decomposition method (DDM), perfectly matched layers (PMLs), and domain reduction method (DRM), in addition to parallel computing capabilities to accelerate the solution of large-scale problems. In this work, the authors provide a detailed description of the implementation for addressing SSI modeling, validate some of the SVL’s features needed for such purpose, and demonstrate that the coupled DRM–PML technique is a necessary condition for accurately solving SSI problems. It is expected that SVL provides a significant contribution to the SSI research community, offering a self-contained and versatile alternative. The software’s practical application in analyzing SSI and directionality effects on 3D structures under seismic loading demonstrates its capability to model real-world earthquake responses in structural engineering.

Keywords: finite element program; soil–structure interaction; perfectly matched layer; domain reduction method; high-performance computing

MSC: 74S05; 74H15; 74G15



Citation: Kusanovic, D.S.; Seylabi, E.E.; Ayoubi, P.; Nguyen, K.T.; Garcia-Suarez, J.; Kottke, A.R.; Asimaki, D. *Seismo-VLAB: An Open-Source Software for Soil–Structure Interaction Analyses*. *Mathematics* **2023**, *11*, 4530. <https://doi.org/10.3390/math11214530>

Academic Editors: Joaquim Infante Barbosa and José Alberto Rodrigues

Received: 30 September 2023

Revised: 24 October 2023

Accepted: 30 October 2023

Published: 3 November 2023



Copyright: © 2023 by the authors. Licensee MDPI, Basel, Switzerland. This article is an open access article distributed under the terms and conditions of the Creative Commons Attribution (CC BY) license (<https://creativecommons.org/licenses/by/4.0/>).

1. Introduction

In the fields of structural and geotechnical engineering, the finite element method (or FEM, see [1–4], to name a few) is the preferred approach for approximating both linear and nonlinear responses of structures [5]. The literature consistently demonstrates that the FEM can effectively replicate the responses of physical experiments (e.g., [6–8]) as well as real-world monitored structures (e.g., [9–11]) with a high degree of accuracy. Unsurprisingly, powerful commercial software such as MSC Nastran [12], ANSYS [13], ABAQUS [14], or LS-DYNA [15] offers several sophisticated material and element libraries for modeling complex structural systems. Nevertheless, in practical civil engineering

applications, it is common to lean towards the use of commercial software such as ETABS, Perform3D, SAP2000 [16–18], and FLAC [19] to handle this particular task. Typically, these software enable the modeling of the structural components with limited (usually elastic) soil materials, if they offer any. Unfortunately, these software usually fail to adequately account for wave propagation in semi-infinite domains, a critical aspect in SSI analyses. For example, the celebrated domain reduction method (or DRM, see [20–22]) proposed by Bielak et al., a powerful approach for modeling semi-infinite domains under remote excitation, is rarely available in commercial software. Similarly, the implementation of absorbing boundary conditions, such as perfectly matched layers (or PML, see [23–25]), to mitigate spurious wave reflections from far-field boundaries is often absent or limited.

The lack of numerical tools for appropriate modeling SSI problems has increased software development during the last two decades. Some software examples are Mastodon [26], Code_Aster [27], ACS-SASSI [28], Real-ESSI [29], and OpenSEES [30], to name a few. These platforms have contributed significantly by providing some capabilities to address the aforementioned limitations. However, it is worth noting that while these open-source software offers important features, several present practical challenges for users. For instance, certain software packages can be difficult to install, modifying their source code can be a formidable task due to a lack of proper comments within the source files, or implementing new features becomes cumbersome due to the source code length. Moreover, running SSI simulations with such software can often prove to be time-consuming and resource-intensive. Motivated by this need, the authors developed *Seismo-VLAB* (or *SVL*, as referenced in [31,32]), an open-source software designed to perform SSI simulations. *SVL* is developed with a focus on simplicity and good coding practices. It incorporates the Eigen C++ Template library [33], which makes it easy for users to make modifications. Additionally, implementations prioritize straightforward methods, avoiding complexity, excessive parameters, local variables, and overuse of multiple inheritances, ensuring straightforward code modifications. While *SVL* was initially created to solve computationally efficient wave propagation for earth dam problems, topographic amplification, and basin effects, it has been extended to incorporate other systems, such as building clusters and lifelines. The most important features of the software include perfectly matched layers as absorbing boundaries [24,25,34]; domain reduction for modeling wavefield incoherency in truncated domains [21]; domain decomposition for optimal parallel computing [35]; material and geometric nonlinearity [36–38]; and interfaces with message passing interface (or MPI, see [39]) and open multi-processing (or OpenMP, see [40]) parallelization.

It is believed that *SVL*'s features are necessary for efficiently solving SSI problems regarding (1) modeling of spatial variability of soil properties for uncertainty quantification in linear and nonlinear models of engineering structures [41–46], (2) inverse problems for parameter estimation as well as reliability-based performance analysis in nonlinear finite element models of engineering structures [31,47–53], (3) site response analysis for the study of amplification or deamplification of seismic waves considering topographic and basin effects [54–62], and (4) specific topics concerning SSI models with time lag effects [63], 3D seismic wave propagation [64], seismic fragility and demand hazard analyses for earth slopes [65], coupled FEM techniques for SSI analyses [66], and earthquake-induced structural pounding between buildings [67]. Thus, *SVL*'s innovativeness lies in its open-source nature, integration of advanced techniques, parallel computing capabilities, modeling of wave propagation in half-spaces, user friendliness, versatility, and applicability to diverse SSI scenarios. This combination makes *SVL* a valuable and pioneering tool for researchers and engineers in the field of soil–structure interaction. In fact, a few researchers have already used *SVL* in some peer-reviewed journals (see [68–72] as examples) for such purpose.

This work describes the most important feature requirements implemented in *SVL* for modeling half-spaces in homogeneous and heterogeneous media. A particular emphasis is placed on (a) the domain decomposition for parallel execution in cases involving large domains and (b) the symmetric hybrid PML formulation and its implementation using the Newmark-beta implicit time integration scheme. This implementation is subjected to

rigorous verification by comparing results between Seismo-VLAB truncated domains with PML against those from enlarged domains with fixed boundaries. Lastly, the DRM implementation, a critical approach for modeling semi-infinite domains, is carefully examined. A comprehensive verification process follows comparing DRM-generated free-field responses with solutions from existing literature. The study concludes by utilizing the coupled DRM–PML method and the parallel computing capabilities of Seismo-VLAB to investigate SSI effects on site and structural responses for a 3D linear elastic building subjected to seismic excitation at various angles of incidence. The later application showcases the software’s capability to model real-world earthquake responses in structural engineering and how these features can help to solve SSI problems in other research areas efficiently.

2. Implementation and Verification for Modeling Half-Space

Seismo-VLAB consists of two primary and self-contained processes: the Pre-Analysis and the Run-Analysis, which are depicted in Figure 1.

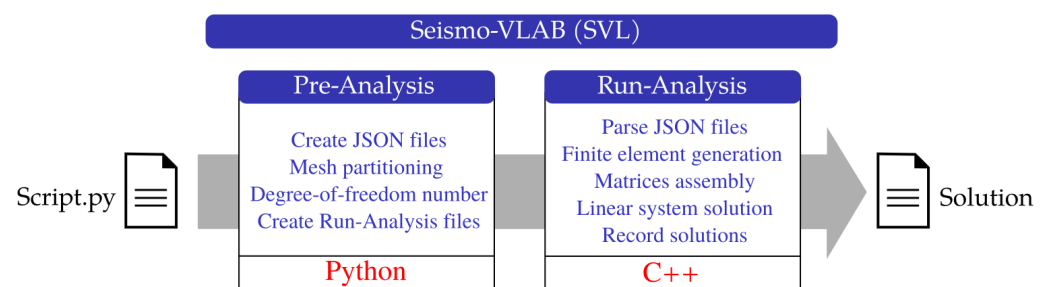


Figure 1. Seismo-VLAB global software structure. The Pre-Analysis is an interface to provide the files to be executed, and the Run-Analysis is the main core that performs the finite element analysis. The Pre-Analysis main task is to transform the Script.py into JSON input files for the Run-Analysis, which in turn converts this information into objects and executes the simulation.

The Pre-Analysis allows users to create, import, adjust, and manipulate FE models, encouraging the development of complex geometries. However, users are required to manually provide node, material, section, and element or utilize external tools to prepare this information for storage in JSON files. Conversely, the Run-Analysis performs the FE analysis, encompassing tasks such as matrix generation, assembly, linear system solution, and stores the solution. Specifically, the Run-Analysis offers the following elements:

- Linearized solid and structural elements such as two- and three-node truss (i.e., `lin2DTruss2`, `lin2DTruss3`, `lin3DTruss2`, and `lin3DTruss3`), three- and six-node triangular (i.e., `lin2DTria3` and `lin2DTria6`), four- and eight-node quadrilateral (i.e., `lin2DQuad4` and `lin2DQuad8`), four- and ten-node tetrahedron (i.e., `lin3DTetra4` and `lin3DTetra10`), eight- and twenty-node hexahedron (i.e., `lin3DHexa8` and `lin3DHexa20`), two-node frame (i.e., `lin2DFrame2` and `lin3DFrame2`), and four-node shell (i.e., `lin3DShell4`) elements are currently available.
- Finite kinematics solid and structural elements such as two-node truss (i.e., `kin2DTruss2` and `kin3DTruss2`), four-node quadrilateral (i.e., `kin2DQuad4`), eight-node hexahedron (i.e., `kin3DHexa8`), and two-node frame (i.e., `kin2DFrame2` and `kin3DFrame2`) elements currently allow large deformation [3,73,74].
- The perfectly matched layer (PML) can be specified for emulating semi-infinite half-spaces in 2D and 3D simulations. Currently, four- and eight-node quadrilateral (`PML2DQuad4` and `PML2DQuad8`), and eight- and twenty-node hexahedron (`PML3DHexa8` and `PML3DHexa20`) elements are implemented.

The element’s properties are computed using numerical integration. This process allows the selection of various quadrature rules, such as Gauss–Legendre and Gauss–Lobatto. Depending on the specific element type, the number of integration points can be chosen within a defined range: 1 to 7 for line elements (e.g., `lin3DTruss2`, `lin3DTruss3`,

lin3DFrame2), 1 to 49 for area elements (e.g., lin2DTria6, lin2DQuad4, lin3DShell4, PML2DQuad4), and 1 to 343 for volume elements (e.g., lin3DTetra10, lin3DHexa8, PML-3DHexa8). This selection considers a uniform grid of points for integration.

Technical details regarding the SVL software's architecture, functionalities, and scalability are presented in [32]. This section presents the essential ingredients a numerical software (or toolbox) must have to perform parallel SSI simulations. In particular, it is demonstrated that the domain decomposition, domain reduction method, and absorbing boundary conditions are necessary to simulate truncated half-space behavior properly.

2.1. Domain Decomposition

Domain decomposition is employed to perform a parallel execution. Here, the model domain (i.e., group of objects such as Node, Element, Material, Section, and Load) is divided so that the number of elements is almost uniform across processors. The aim of performing the mesh partitioning with Metis [35] is to minimize the load imbalance [75] by distributing roughly the same number of elements across processors. However, other graph partitioning programs such as SCOTCH [76] or Zoltan [77] can be incorporated to reach the same purpose.

2.1.1. Implementation

A hypergraph, denoted as $\mathcal{H} = (\mathcal{X}, \mathcal{E})$, consists of a set of vertices, represented by \mathcal{X} , and hyperedges, represented by \mathcal{E} . In this structure [78], every hyperedge is essentially a subset of the set of vertices \mathcal{X} . In this regard, the k -way hypergraph partitioning problem is defined as follows: given a hypergraph $\mathcal{H} = (\mathcal{X}, \mathcal{E})$, partition set \mathcal{X} into k disjoint subsets, i.e., $\mathcal{X}_1, \mathcal{X}_2, \dots, \mathcal{X}_k$, such that $\mathcal{X} = \bigcup_{j=1}^k \mathcal{X}_j$. The reader may refer to [79] for more details on how this is performed. The hypergraph \mathcal{H} is constructed internally using Metis subroutines, where the vertices \mathcal{X} and edges \mathcal{E} data in SVL are generated using the Mesh element's connectivity information. In order to minimize the processor load imbalance, a weight is specified for each vertex proportional to the number of degrees of freedom (N_{dof}^n) of each Node. Thus, the element's load, computed as the square of the number of nodes multiplied by the number of degrees of freedom, offers an approximate measure of the computational complexity required to calculate a matrix. The latter gives a rough estimation of the relative load of an element compared to others, allowing for clustering groups of elements where the sum of individual loads is similar. This process is performed using the k -way hypergraph partitioning in Metis, from which the information is collected to construct the subdomains to be distributed to each processor. The OpenMPI [40,80–82] interface allows each partition to be sent to different processor units, so that the element mass $\mathbf{M}^e \in \mathbb{R}^{N_{\text{dof}}^e \times N_{\text{dof}}^e}$, damping $\mathbf{C}^e \in \mathbb{R}^{N_{\text{dof}}^e \times N_{\text{dof}}^e}$, and stiffness $\mathbf{K}^e \in \mathbb{R}^{N_{\text{dof}}^e \times N_{\text{dof}}^e}$ matrices, and force $\mathbf{F}^e \in \mathbb{R}^{N_{\text{dof}}^e}$ vector (N_{dof}^e is the total number of degrees of freedom of the e -th element) can be generated for each subdomain. The contribution to the global stiffness matrix and force vector is assembled locally. However, the full assembly to the stiffness matrix $\mathbf{K}_{\text{eff}} \in \mathbb{R}^{N_{\text{free}} \times N_{\text{free}}}$ and force vector $\mathbf{F}_{\text{eff}} \in \mathbb{R}^{N_{\text{free}}}$ (N_{free} is the number of free degrees of freedom) is handled by PETSc [83–85] and MUMPS [86,87] APIs.

2.1.2. Verification

The verification case considers a 3D SSI model. The soil domain size has, approximately, a horizontal length $100 \times 100 \text{ m}^2$ and a vertical length 90 m. This domain is discretized using 121,944 Node, 105,825 Element, 25 Material, and 26,247 Constraint objects that allow for tying together both PML/soil and shells/soil element interfaces. Similarly, the building model size is approximately $50 \times 50 \text{ m}^2$ in plan view and 60 m in elevation. The building domain is discretized using 7861 Node, 9552 Element, and 19 Section objects in total. The 3D linearized eight-node hexahedron (i.e., lin3DHexa8) elements to model the soil, and 3D linearized eight-node hexahedron perfectly matched layer (i.e., PML3DHexa8) elements to truncate the semi-infinite half-space, are employed. Moreover, 3D linearized two-node beam (i.e., lin3DFrame2) and 3D linearized four-node shell (i.e.,

lin3DShe114) elements are employed to model the building slabs, walls, columns, and beams. The finite element mesh partition is shown in Figure 2 for five (left) and eleven (right) processors, respectively. This figure also shows how elements are uniformly clustered, leading to similar colored volumes. The partitioning process does not enhance the solution's accuracy; its impact is mainly on performance in terms of execution time. Parallel simulations generally outpace their serial counterparts, making clustering, especially in linear analysis cases, beneficial for faster computation of element vectors and matrices as well as solving linear systems handled by the MUMPS and PETSc APIs.

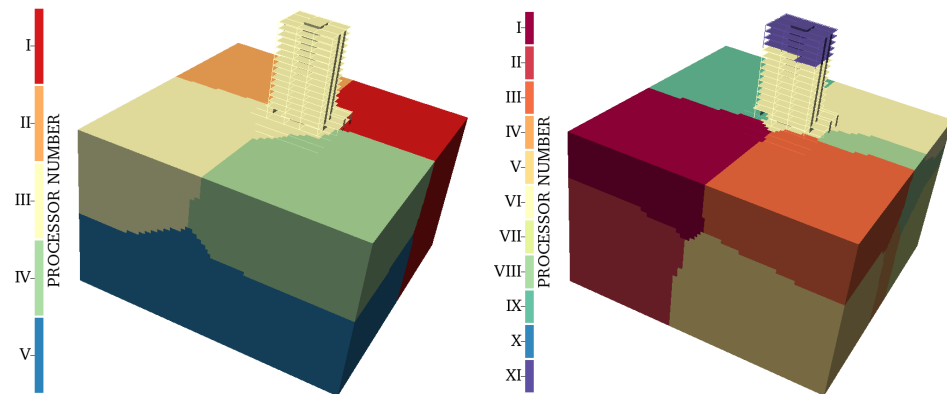


Figure 2. Domain decomposition of a 3D SSI building model using 5 (left) and 11 (right) processors.

2.2. Domain Reduction Method

The boundary element methods (BEMs) and their variants have been extensively used to investigate the problems where incident plane waves (P, SV, SH, Rayleigh) interact with canyons, basins, and buildings [88–92]. However, the majority of research efforts have focused on analyzing simple topographies and homogeneous half-spaces, which provide an oversimplified representation of the soil domain in reality. Moreover, the problem is solved in the frequency domain, making it challenging to incorporate the nonlinear behavior of both soil and structures. Currently, substructure and direct approaches employing the FEM are the most commonly used techniques for studying SSI effects. In particular, the direct approach has proven to be enormously powerful since complex foundation shapes and nonlinear responses of soil and structure are explicitly taken into account. However, one of the main problems in the direct approach is to specify consistent input ground motions inside the near field [93,94]. In general, this process involves using an FE model with enlarged domains to simulate the transition of seismic waves from far field to near field. However, addressing the near field is challenging due to the need for an accurate FE mesh that represents topographic characteristics and local soil variations. This leads to a computationally demanding task to model interactions among the structure, foundation, and soil. In this regard, the DRM developed by [21] is an effective FE methodology for modeling earthquake ground motion in highly heterogeneous localized regions.

One of the most remarkable capabilities of SVL is its approach for modeling the propagation of a plane wave in layered media for site amplification and 3D SSI problems in the time domain. This approach comprises two main steps: (i) the displacement fields of the incident waves in layered soils are initially obtained by, e.g., the stiffness matrix method (SMM) or thin layer method (or TML, see [95]); and (ii) these signals are subsequently fed into the domain reduction method (or DRM, as described in [21,22]), enabling the computation of effective input nodal forces for FE models. This approach, implemented in SVL, offers several advantages: (i) it can be applied to horizontally layered soil media and any topographical features inside the DRM layer, such as complex 3D shapes of embedded foundations, canyons, and basins; (ii) the analyses are performed in the time domain, which facilitates the use of contact interfaces and nonlinear material models; and (iii) by using DRM to map incoming waves from the far-field to the near-field domain, along

with absorbing boundaries, the computational cost is significantly reduced. The proposed method is presented in more detail in [69] for the case of Rayleigh waves. This section briefly describes the framework for simulating P and SV waves in layered media using SMM and DRM.

2.2.1. Implementation

The proposed methodology to simulate SV wave propagation in layered media using FEM in the time domain is described below. Note that the process for P waves is identical, except for different polarization and wave velocities.

- (a) Choose a reference incoming signal $f_0(x_0, y_0, t)$ at a reference point (x_0, y_0) , propagating at an angle θ with respect to vertical axis. This time series can be a predefined or a recorded signal during a seismic event. For example, incoming signals can be obtained from the PEER Ground Motion Database, hosted at <https://ngawest2.berkeley.edu/> (accessed on 2 May 2023); see [96] for details. This task is not difficult when considering linear elastic homogeneous and inhomogeneous half-space.
- (b) Transform the reference signal into the frequency domain by applying the fast Fourier transform (FFT). Denote $\hat{f}_{0,j}(x_0, y_0, \omega_j)$ as the component of the transformed signal corresponding to discrete angular frequency ω_j .
- (c) Calculate horizontal displacement $\hat{u}(x_0, y, \omega) = \{\hat{u}_j(x_0, y, \omega_j)\}$ and vertical displacement $\hat{v}(x_0, y, \omega) = \{\hat{v}_j(x_0, y, \omega_j)\}$ using SMM, which is described later on.
- (d) Compute the horizontal displacement $\hat{u}(x, y, \omega) = \hat{u}_j(x, y, \omega_j)$ and vertical displacement $\hat{v}(x, y, \omega) = \hat{v}_j(x, y, \omega_j)$ at the DRM nodes. These free-field displacements for each ω_j are determined as follows:

$$k_j = \frac{\omega_j \sin \theta}{V_s}, \text{ and } \begin{bmatrix} \hat{u}_j(x, y, \omega_j) \\ \hat{v}_j(x, y, \omega_j) \end{bmatrix} = \begin{bmatrix} \hat{u}_j(x_0, y, \omega_j) \\ \hat{v}_j(x_0, y, \omega_j) \end{bmatrix} \exp(-i k_j(x - x_0)), \quad (1)$$

where k_j is the horizontal wavenumber, i is the imaginary number, and $i^2 = -1$. The exponential term $\exp(-i k_j(x - x_0))$ represents the phase lag due to finite horizontal apparent velocity when the SV wave travels through a distance $(x - x_0)$.

- (e) Use inverse FFT to obtain the time histories of those displacements, $u(x, y, t)$ and $v(x, y, t)$.
- (f) Calculate the effective input forces for the FEM model using DRM.
- (g) Apply those input forces at the corresponding locations of the DRM layer and perform the FEM analysis.

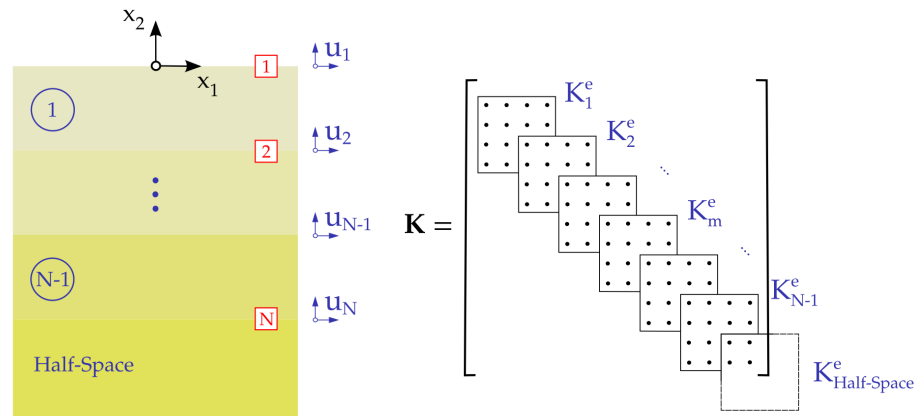
The SMM needed in (c) is now described for a layered medium with N interfaces, i.e., $N - 1$ layers over a homogeneous half-space. In Figure 3a, the displacements at interfaces are obtained by solving the following system of equations:

$$\begin{bmatrix} \mathbf{K}_{11} & \mathbf{K}_{12} & \cdots & \mathbf{0} \\ \mathbf{K}_{21} & \mathbf{K}_{22} & \ddots & \vdots \\ \mathbf{0} & \ddots & \ddots & \mathbf{K}_{N-1,N} \\ \mathbf{0} & \cdots & \mathbf{K}_{N,N-1} & \mathbf{K}_{NN} + \mathbf{K}_{\text{half}} \end{bmatrix} \begin{bmatrix} \mathbf{u}_1 \\ \mathbf{u}_2 \\ \vdots \\ \mathbf{u}_N \end{bmatrix} = \begin{bmatrix} \mathbf{0} \\ \vdots \\ \mathbf{0} \\ \mathbf{K}_{\text{full}} \mathbf{u}_{\text{full}}^* \end{bmatrix}, \quad (2)$$

where \mathbf{K}_{ij} , \mathbf{K}_{half} , and \mathbf{K}_{full} are the 2×2 component stiffness matrices of a soil layer, half-space, and imaginary full space (by joining two half-spaces), respectively; \mathbf{u}_k with $1 \leq k \leq N$ is the displacement vector at the k -th interface; and $\mathbf{u}_{\text{full}}^*$ is the displacement vector at the surface location of the half-space given free propagation of plane waves in the imaginary full space. For each frequency ω_j , $\mathbf{u}_{\text{full}}^*$ is calculated as

$$\mathbf{u}_{\text{full}}^* = \begin{bmatrix} \cos \theta \\ i \sin \theta \end{bmatrix} \hat{f}_{0,j}(x_0, y_0, \omega_j) \exp\left(-i \frac{\omega_j \cos \theta}{V_s} (y_N - y_0)\right), \quad (3)$$

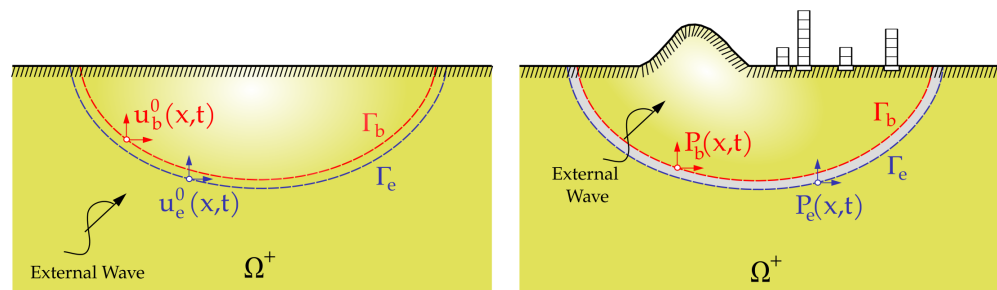
where y_N is the y-coordinate of the half-space surface. Figure 3b illustrates the assembly of the element stiffness matrices of soil layers required to form the global stiffness matrix. Once the motions at the interfaces are obtained, the displacements at the interior of the soil layer are calculated by means of analytic continuation. Interested readers can refer to [95] for further details.



(a) Layered soil media (b) Assembly of element matrices

Figure 3. Conceptual representation of the stiffness matrix method used for free-field motion.

The derived free-field motions represented in Figure 4a (i.e., displacements, velocity, and acceleration) are subsequently used to calculate effective input forces for the FEM simulations, as is represented in Figure 4b. The generated free-field motion files can be provided in SVL as plain text files with columns specifying displacement, velocity, and acceleration for each component.



(a) Free-field wave propagation (b) Effective forces applied to the near field

Figure 4. The domain reduction method schematic representation.

The effective input forces \mathbf{P}^{eff} vector acting within the layer of elements is

$$\mathbf{P}^{\text{eff}} = \begin{bmatrix} \mathbf{p}_i^{\text{eff}} \\ \mathbf{p}_b^{\text{eff}} \\ \mathbf{p}_e^{\text{eff}} \end{bmatrix} = \begin{bmatrix} \mathbf{0} \\ -\mathbf{M}_{be}^{\Omega^+} \ddot{\mathbf{u}}_e^0 - \mathbf{C}_{be}^{\Omega^+} \dot{\mathbf{u}}_e^0 - \mathbf{K}_{be}^{\Omega^+} \mathbf{u}_e^0 \\ \mathbf{M}_{eb}^{\Omega^+} \ddot{\mathbf{u}}_b^0 + \mathbf{C}_{eb}^{\Omega^+} \dot{\mathbf{u}}_b^0 + \mathbf{K}_{eb}^{\Omega^+} \mathbf{u}_b^0 \end{bmatrix}, \tag{4}$$

where the subscripts i, b, and e denote the regions corresponding to the interior of the designated domain, the boundary, and the area outside the DRM layer. The matrices \mathbf{M}^{Ω^+} , \mathbf{C}^{Ω^+} , and \mathbf{K}^{Ω^+} represent the portions of the mass, damping, and stiffness matrices that are situated off the main diagonal. These matrices are constructed using the data from the DRM layer positioned between two boundaries denoted as Γ_b and Γ_e . Lastly, \mathbf{u}^0 , $\dot{\mathbf{u}}^0$, and $\ddot{\mathbf{u}}^0$ are the free-field displacements, velocity, and acceleration of the background layered soil. These forces are computed internally at the element level using the `Element::ComputeDomainReductionForces()` member function, which returns the $\mathbf{P}^{\text{eff}} \in \mathbb{R}^{N_{\text{dof}}}$ force vector to be assembled.

The propagation of plane waves (P, SV, Rayleigh) in a 3D space is readily determined by recognizing that, at a specific moment in time, the spatial variation remains constant across a plane that is perpendicular to the direction of propagation. As illustrated in Figure 5, the displacement fields within any 3D coordinate system (x_1, x_2, x_3) are derived through a rotation matrix,

$$\mathbf{u}(x_1, x_2, x_3) = \begin{bmatrix} u \\ v \\ w \end{bmatrix} = \begin{bmatrix} \cos \varphi & \sin \varphi & 0 \\ -\sin \varphi & \cos \varphi & 0 \\ 0 & 0 & 1 \end{bmatrix} \begin{bmatrix} u_1 \\ 0 \\ u_2 \end{bmatrix}, \tag{5}$$

where φ is the azimuth angle, $\mathbf{u}(x_1, x_2) = (u_1, u_2)$ is the free-field motion in 2D, and $\mathbf{u}(x_1, x_2, x_3) = (u, v, w)$ is the free-field motion in 3D, respectively.

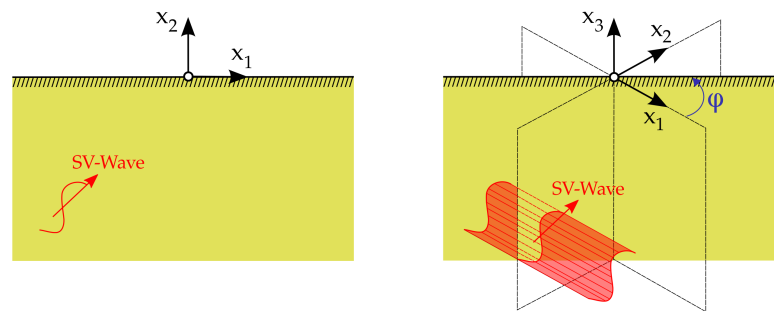


Figure 5. Displacement, velocity, and acceleration mapping from 2D to 3D coordinate systems.

2.2.2. Verification

The DRM implementation in SVL is demonstrated, and the solution is verified using solutions presented in [55,97,98].

A 3D soil domain with a horizontal length of $120 \times 120 \text{ m}^2$ and a vertical length of 80 m is considered. Within this domain, isotropic linear elastic materials, characterized by a density of $\rho_s = 2000 \text{ kg/m}^3$ and Poisson’s ratio of $\nu_s = 0.25$, are employed. The DRM is used to transmit the ground motion generated by an in-plane SV wave propagating within the near field at an angle of 15° degrees. The incident ground motion is defined using a Ricker function similar to Equation (15). This numerical example considers a central frequency of $f_0 = 2.0 \text{ Hz}$ and shear wave velocity of $V_s = 120 \text{ m/s}$. Three control points at coordinates $P_1 = (-40, -40, 0)$, $P_2 = (40, 40, -60)$ and $P_3 = (40, 40, 0)$ are selected for the purpose of comparing the time series with results presented in [55]. The model has 87,778 nodes, 25,635 restrains, and 100,335 elements divided into 73,728 3D linearized eight-node hexahedron elements (i.e., `lin3DHexa8`) used to discretized the linear and elastic soil domain, and 25,635 1D two-node zero-length elements (i.e., `ZeroLength1D`) placed along the boundary to absorb possible scatter waves. The simulation time is set to be $T_{\text{sim}} = 4.0 \text{ s}$, with a temporal discretization of $\Delta t = 0.004 \text{ s}$, leading to a number of $n_t = 1001$ time steps. The simulation is performed using three processors, and an execution time of 68 min is required to complete the simulation on a Lenovo laptop equipped with an Intel(R) Core(TM) i7-4720HQ CPU running at 2.60 GHz and `x86_64` architecture.

Figure 6 displays the velocity time series comparison at the three control points. The results show a perfect agreement with the solution presented in [55,97,98] for each component. In addition, Figure 7 shows the velocity amplitude field at (a) $t = 2.0 \text{ s}$, (b) $t = 2.5 \text{ s}$, and (c) $t = 3.0 \text{ s}$. Since the truncated soil domain, in this case, has no features that can generate scattering waves, the near-field response has to match the free-field conditions imposed at the DRM elements. This fact demonstrates the proper implementation of DRM in 3D settings in SVL. The reader should note that the DRM implementation is correct, since the wave field is fully contained in the DRM box. A wrong implementation will generate scatter waves outside the DRM layer of elements represented by the blue volume in Figure 7. In this regard, the lysmer dashpots will not be

enough to absorb the scattered field efficiently due to the proximity of the wave field to the boundaries.

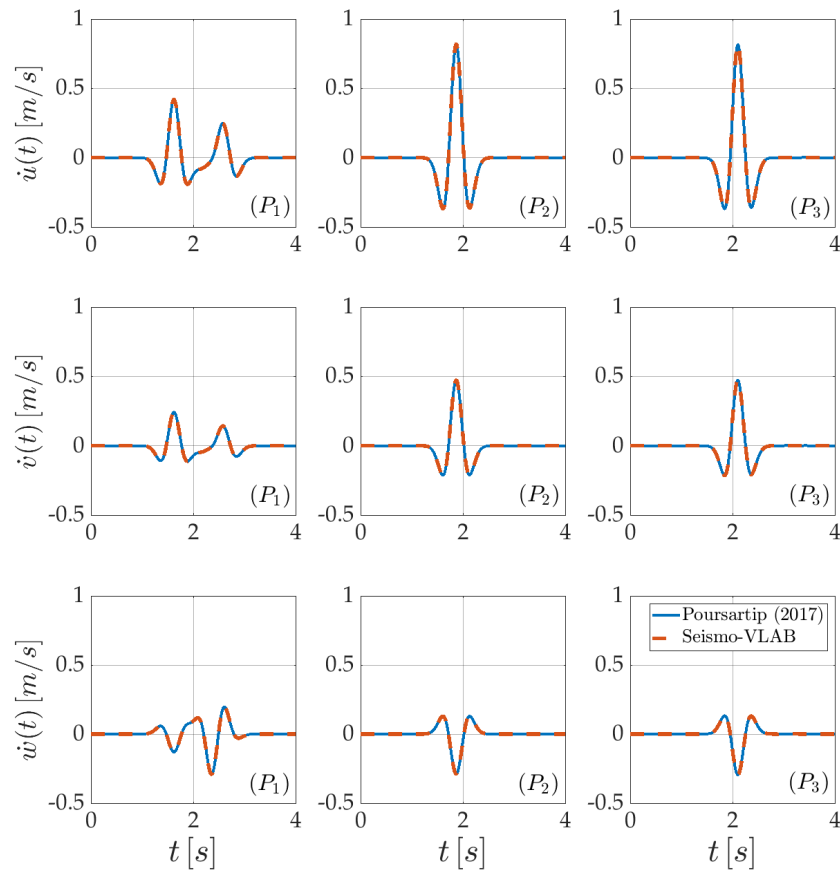


Figure 6. Timeseries of the 3D velocity vector field components u , v , and w computed using the DRM at the control points P_1 , P_2 , and P_3 for an inclined wave at an incident angle of 15° degrees in a homogeneous half-space.

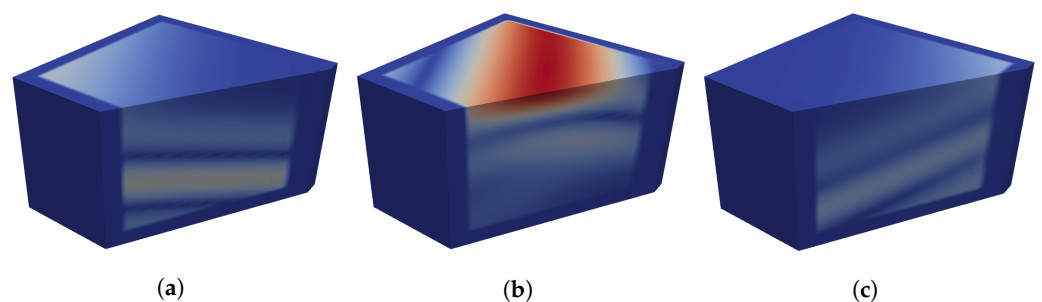


Figure 7. Snapshots of the 3D velocity amplitude field computed at time steps (a) $t = 2.0$ s, (b) $t = 2.5$ s, and (c) $t = 3.0$ s using the DRM load modeling for an inclined wave at an incident angle of 15° degrees in a homogeneous half-space. The red and blue colors represent a velocity magnitude of 1 m/s and 0 m/s, respectively.

2.3. Absorbing Boundary Conditions

Seismo-VLAB offers perfectly matched layer (PML) functionality for simulating semi-infinite half-spaces in both 2D and 3D simulations. Currently, the software includes implementations of various PML elements, such as 2D linearized four-node quadrilateral (PML2DQuad4), 2D linearized eight-node quadrilateral (PML2DQuad8), 3D linearized eight-node hexahedron (PML3DHexa8), and 3D linearized twenty-node hexahedron (PML3DHexa20).

These implementations are based on fully mixed symmetric formulations presented in [24,25,99] for plane-strain (2D) and 3D settings.

2.3.1. Implementation

The key idea in PML is the use of complex coordinate stretching. The complex coordinate stretching function in direction s , which can be x , y , or z directions in the Cartesian coordinate system, is defined as

$$\epsilon_s(s, \omega) = \alpha_s(s) + \frac{\beta_s(s)}{i\omega}, \tag{6}$$

where i is the imaginary number, and α_s and β_s are scaling and attenuation functions, defined as

$$\alpha_s(s) = \begin{cases} 1 & 0 \leq s \leq s_0 \\ 1 + \frac{(m+1)b}{2L_{pml}} \log \frac{1}{R} \left[\frac{(s-s_0)n_s}{L_{pml}} \right]^m & s_0 \leq s \end{cases}, \tag{7}$$

$$\beta_s(s) = \begin{cases} 0 & 0 \leq s \leq s_0 \\ \frac{(m+1)V_{ref}}{2L_{pml}} \log \frac{1}{R} \left[\frac{(s-s_0)n_s}{L_{pml}} \right]^m & s_0 \leq s \end{cases}, \tag{8}$$

where m is the user-defined degree of the stretching polynomial; n_s is the s -th component of the outward normal to the interface between the PML region and the regular (soil) domain (Figure 8); L_{pml} is the thickness of the PML region in the s direction (Figure 8); s_0 is the s -th component of the reference point where stretching is defined; b is a characteristic length, set to $L_{pml}/10$; V_{ref} is a reference velocity, set to be the P wave velocity; and R is a user-defined reflection coefficient.

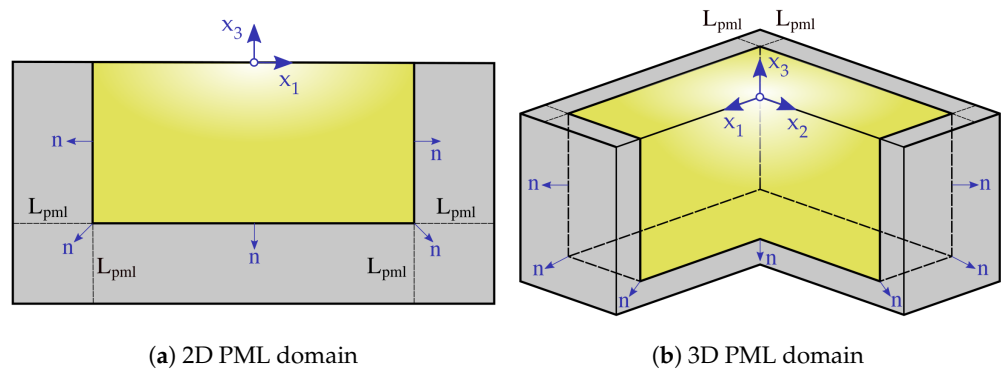


Figure 8. Illustration of PML domain attached to the soil domain. The soil domain is represented in yellow, whereas the PML domain is represented in grey.

The weak form of the PML formulation presented in [24,99] yields a second- and a third-order ODE, respectively, for the governing equation of motion, with a mixed free variable \mathbf{U} consisting of both displacement and stress fields. The second-order ODE arising in the plane-strain PML problems can be solved seamlessly using conventional numerical time integration methods such as the Newmark-beta method. For solving the third-order ODE of the 3D PML problems, i.e.,

$$\mathbf{M}\ddot{\mathbf{U}}_{n+1} + \mathbf{C}\dot{\mathbf{U}}_{n+1} + \mathbf{K}\mathbf{U}_{n+1} + \mathbf{G}\mathbf{U}_{n+1} = \dot{\mathbf{R}}_{n+1}^{(i)}. \tag{9}$$

Fathi et al. [99] suggested using the extended Newmark-beta method. This requires introducing an internal state variable $\bar{\mathbf{U}} = \int \mathbf{U}dt$ to reduce the order of the third-order

ODE, such that $\mathbf{M} \ddot{\mathbf{U}}_{n+1} + \mathbf{C} \dot{\mathbf{U}}_{n+1} + \mathbf{K} \mathbf{U}_{n+1} + \mathbf{G} \bar{\mathbf{U}}_{n+1} = \mathbf{R}_{n+1}^{(i)}$, and approximating the mixed response field and their derivatives as follows:

$$\bar{\mathbf{U}}_{n+1} = \bar{\mathbf{U}}_n + \Delta t \mathbf{U}_n + \frac{\Delta t^2}{2} \dot{\mathbf{U}}_n + \left(\frac{1}{6} - \beta\right) \Delta t^3 \ddot{\mathbf{U}}_n + \beta \Delta t^3 \ddot{\mathbf{U}}_{n+1}, \tag{10}$$

$$\mathbf{U}_{n+1} = \mathbf{U}_n + \Delta t \dot{\mathbf{U}}_n + \left(\frac{1}{2} - \gamma\right) \Delta t^2 \ddot{\mathbf{U}}_n + \gamma \Delta t^2 \ddot{\mathbf{U}}_{n+1}, \tag{11}$$

$$\dot{\mathbf{U}}_{n+1} = \dot{\mathbf{U}}_n + (1 - \alpha) \Delta t \ddot{\mathbf{U}}_n + \alpha \Delta t \ddot{\mathbf{U}}_{n+1}. \tag{12}$$

This time integration scheme has been implemented in SVL for $(\beta, \gamma, \alpha) = (1/12, 1/4, 1/2)$, which results in solving $\mathbf{K}_{\text{eff}} \Delta \mathbf{U} = \mathbf{F}_{\text{eff}}$ with

$$\mathbf{K}_{\text{eff}} = \mathbf{K}_{n+1}^{(i-1)} + \frac{4}{\Delta t^2} \mathbf{M} + \frac{2}{\Delta t} \mathbf{C} + \frac{\Delta t}{3} \mathbf{G}, \tag{13}$$

$$\mathbf{F}_{\text{eff}} = \mathbf{R}_{n+1}^{(i)} - \mathbf{F}_{n+1}^{(i-1)} + \mathbf{M} \left(\frac{4}{\Delta t} \dot{\mathbf{U}}_n + \ddot{\mathbf{U}}_n \right) + \mathbf{C} \dot{\mathbf{U}}_n - \mathbf{G} \left(\bar{\mathbf{U}}_n + \Delta t \mathbf{U}_n + \frac{\Delta t^2}{6} \ddot{\mathbf{U}}_n \right). \tag{14}$$

The matrix \mathbf{G} is the PML history matrix, $\mathbf{R}_{n+1}^{(i)}$ is the external force vector, $\mathbf{F}_{n+1}^{(i-1)}$ is the internal force vector, and i is the nonlinear iteration step. The structures and explicit forms of the PML matrices are omitted, but they can be found in [24,25,99].

2.3.2. Verification

The PML implementation in SVL is demonstrated, and the solution is verified using enlarged domain solutions.

A 3D soil domain with a horizontal length of $150 \times 150 \text{ m}^2$ and vertical length of 100 m is considered. Within this domain, isotropic linear elastic materials for the soil, characterized by a density of $\rho_s = 2000 \text{ kg/m}^3$ and Poisson’s ratio of $\nu_s = 0.25$, are considered. In addition, a PML zone of 20 m thickness is placed next to the truncated domain. A downward point load $F(t)$, applied at the center of the free surface, is prescribed as an effective force Ricker function, proportional to Equation (15):

$$F(t) = \left(1 - 2(\pi f_0)^2(t - t_0)^2\right) \exp\left(-(\pi f_0)^2(t - t_0)^2\right). \tag{15}$$

In this numerical example, a central frequency of $f_0 = 2.0 \text{ Hz}$ and a soil shear wave velocity of $V_s = 200 \text{ m/s}$ are employed. The soil domain is now discretized using 13,500 3D linearized eight-node hexahedron (i.e., 1in3DHexa8) elements, and the PML layer of 25 m is discretized using 18,500 3D linearized eight-node hexahedron perfectly matched layer (i.e., PML3DHexa8) elements. Three control points at coordinates $P_1 = (0, 0, -40)$, $P_2 = (30, 30, -40)$, and $P_3 = (30, 30, 0)$ are defined to compare the time series against results of an enlarged model with fixed boundaries. The simulation is performed using three processors, and the execution time of 16 min is reported using a Lenovo laptop using an Intel(R) Core(TM) i7-4720HQ CPU 2.60 GHz with eight cores and x86_64 architecture.

Figure 9 shows the velocity time series comparison at the three control points P_1 , P_2 , and P_3 , respectively. The results show a perfect agreement with the enlarged model solution. In addition, in Figure 10, the velocity field amplitude for the truncated soil domain at (a) $t = 1.00 \text{ s}$, (b) $t = 1.20 \text{ s}$, and (c) $t = 1.75 \text{ s}$ are displayed, convincingly showing that there are no reflections generated from the boundary and demonstrating the proper implementation of PML in 3D settings in SVL. The reader should note that the PML implementation is correct since the wave field is fully absorbed in the boundaries. A wrong implementation will generate waves that bounce back from the boundaries, noticeable after 2 s in the time series provided.

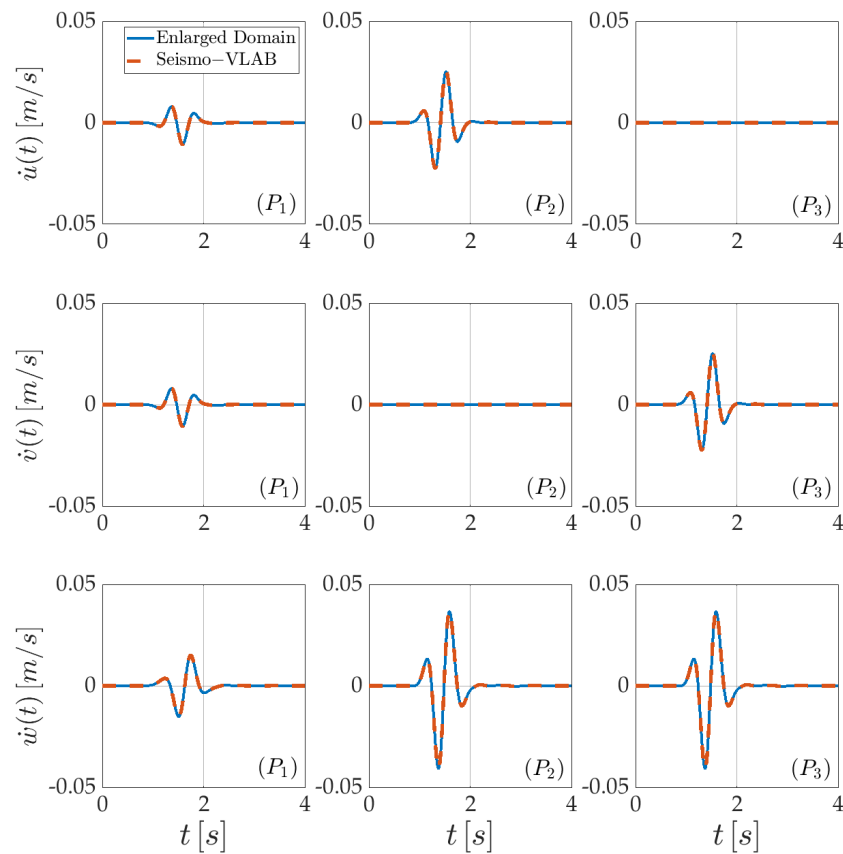


Figure 9. Time series of the 3D velocity vector field components u , v , and w computed using the truncated model using PML at the control points P_1 , P_2 , and P_3 in a homogeneous half-space.

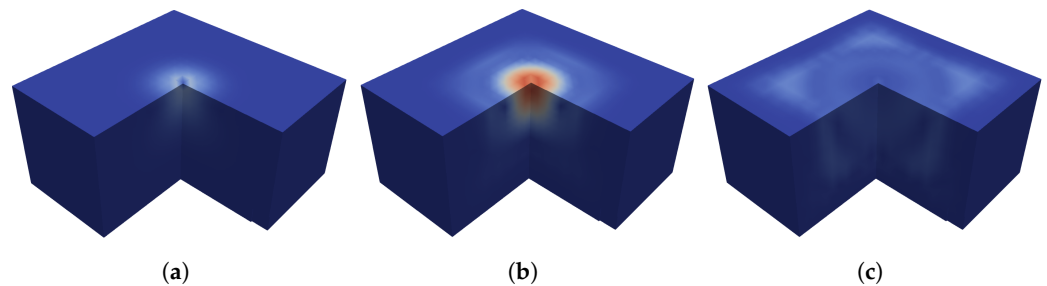
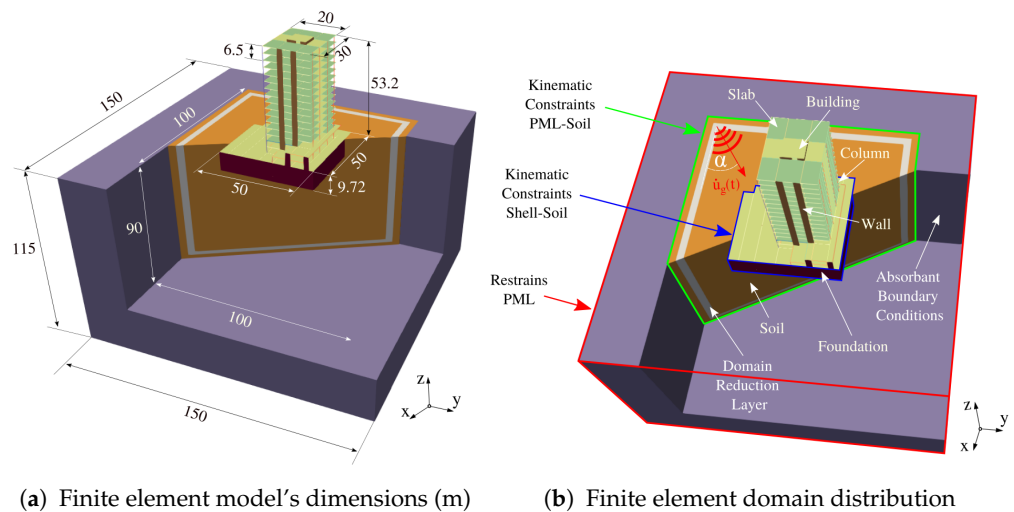


Figure 10. A snapshot of the velocity amplitude field in 3D under vertical loading at the surface of the domain at time steps (a) $t = 1.00$ s, (b) $t = 1.20$ s, and (c) $t = 1.75$ s. The red and blue colors represent a velocity magnitude of 0.05 m/s and 0 m/s, respectively.

3. Evaluation of the SSI Effects on a 3D Building Subjected to a Seismic Excitation for Different Attack Angles

In this application case, the model’s dimension and the domain element’s distribution are depicted in Figure 11. Because the model discretization rendered a large number of elements, a parallel execution for which the same domain’s partition is represented in Figure 2 on the left is considered. For simplicity, and due to the small magnitude of the seismic excitation considered in this analysis, a linearized formulation for the elements and material is assumed. The main goal of this application case is threefold: (a) to showcase some of the relevant features encountered in SSI, (b) to verify that the coupled DRM–PML technique is necessary for accurately solving SSI problems, and (c) to demonstrate SVL’s capacity to model real-world earthquake responses in structural engineering due to directionality effects.



(a) Finite element model's dimensions (m) (b) Finite element domain distribution

Figure 11. Finite element model considered for the evaluation of the SSI effects on a 3D building subjected to a sv seismic excitation. The purple, orange, red, and green volumes represent the PML, soil, foundation, and building domains, respectively. The green, blue, and red line interfaces represent areas where the PML-Soil constraints, Foundation-Soil constraints, and PML restraints are applied, respectively.

The soil domain is a square prism with horizontal lengths of $100 \times 100 \text{ m}^2$ and vertical lengths of 90 m. Standard 3D linearized eight-node hexahedron elements (i.e., `lin3DHexa8`) are employed to discretize the domain. Linear elastic material with properties of $\rho_s = 2000 \text{ kg/m}^3$, $\nu_s = 0.30$, and $V_s = 150 \text{ m/s}$ are considered to describe the soil behavior. A PML zone discretized using a perfectly matched layer of eight-node hexahedron elements (i.e., `PML3DHexa8`) of 25 m thickness is placed next to the boundaries to emulate the half-space condition. On the other hand, the reinforced concrete main tower (superstructure) has sixteen floors with a total height of 53.2 m. The basement (substructure) has three floors designed for parking and is buried -9.72 m below the ground level. The substructure surface area is approximately 2100 m^2 , while the superstructure surface area is approximately 750 m^2 . A core of walls is provided around the elevator to control the horizontal deformations. The reinforced concrete elasticity modulus varies between 20–26 GPa depending on the element, with a density of $\rho_c = 2500 \text{ kg/m}^3$ and Poisson's ratio of $\nu_c = 0.20$. Slabs in the main tower (i.e., from floors 1 through 16) are considered to behave as a rigid diaphragm. The building model is discretized using 3D linearized two-node beam elements (i.e., `lin3DFrame2`) for beams and columns, and 3D linearized four-node shell elements (i.e., `lin3DShe114`) for walls and slabs. As solid elements (i.e., soil) and structural elements (i.e., beams, columns, and shells) have different numbers of degrees of freedom per node, it becomes necessary to establish an indirect coupling between them. To ensure a clean and numerically stable approach, kinematic constraints following the recommendations of [3,100,101] at the contact interface, as illustrated in the blue interface in Figure 11b, are used. In this method, the connections are established by linking the nodes of frame and shell elements with nodes of solid elements solely for translational degrees of freedom (three for each node). Meanwhile, the rotational degrees of freedom (three for each) from beam, column, and shell elements are left unconnected. This sort of connection imposes identical displacements on the soil nodes at the soil–foundation interface; however, some localized deformations in the surrounding soil may be induced using this approach. Therefore, columns at the bottom, as well as the foundation elements, are not in direct contact with the soil (see, Figure 11a interface between the red and orange domain). The same coupling between soil and PML elements is achieved through kinematic constraints on the displacement degree of freedom (see, Figure 11b represented by the green interface). Finally, the rigid diaphragm behavior of the floors is imposed by adding

an auxiliary node with three degrees of freedom (i.e., diaphragm node) and then imposing kinematic constraints on all nodes at the floor level.

The domain reduction method (DRM, represented in Figure 11b by the white layer of soil elements) is used in order to transmit an SV wave ground motion. The input signal is propagated upwards at different angles with respect to the horizontal x -axis. In particular, the angles $\alpha = 0^\circ, 30^\circ, 60^\circ$, and 90° degrees are considered. The incident ground motion velocity $\dot{u}_g(t)$ is a Ricker pulse, expressed as

$$\dot{u}_g(t) = \dot{u}_p \left(1 - 2\gamma(t - t_0)^2 \right) \exp\left(-\gamma(t - t_0)^2\right), \quad (16)$$

where \dot{u}_p is the characteristic value of the pulse velocity, $\gamma = (\pi f_0)^2$, f_0 is the characteristic frequency, and t_0 is the time position where the velocity attains its maximum. In all simulations, a characteristic value of $\dot{u}_p = 10$ cm/s, characteristic frequency of $f_0 = 2.0$ Hz, and a peak velocity time of $t_0 = 1.0$ s are considered. The characteristic frequency f_0 is selected to generate an input signal with frequency content ranging between 0–7.5 Hz, which emulates most real earthquake signals. The simulation time is $T_s = 10.0$ s with a temporal discretization of $\Delta t = 0.002$ s, leading to a time step number of $n_t = 5001$ for the entire simulation. All simulations were carried out in a server with an Intel(R) Xeon(R) CPU E5-2687W v3 3.10 GHz, x86_64 architecture, and 40 CPU cores. Overall, the simulation took 520 min using five partitions (i.e., using only five processors), and employed 35.9 GB in evolving 5001 time steps.

In Figure 12, the first three fixed-base mode shapes for the building are represented. The figure displays the deformed configuration in solid colors, whereas black lines represent the undeformed configuration. In particular, Figure 12a displays a decoupled translational mode shape along the y -direction generated at a fundamental frequency of 0.75 s. On the other hand, Figure 12b shows a coupled translational and rotational mode shape along the x -direction. Note that the coupling is a result of a concrete reinforcement wall on one side, which creates a misalignment between the center of mass and the structural stiffness. The second fixed-base mode shape is obtained at a fundamental frequency of 0.68 s. Finally, Figure 12c illustrates the third fixed-base mode shape, which is purely torsional, vibrating at a frequency of 0.47 s.

In Figure 13, both the velocity field amplitude and deformed configuration at time (a) $t = 1.20$ s, (b) $t = 1.60$ s, (c) $t = 2.32$ s, (d) $t = 3.52$ s, (e) $t = 5.20$ s, and (f) $t = 8.00$ s for $\alpha = 30^\circ$ degrees are displayed. Note how in Figure 13a,b, inside the DRM (near-field) domain, the SV wave propagating upwards is successfully generated. However, because of the building, a scattered field is generated outside the DRM (far-field) domain in Figure 13c–e. In particular, at time $t = 3.52$ s, the wavefront generated by the building due to the so-called inertial interaction is shown. Inertial interaction refers to the displacements and rotations occurring at the foundation level of a structure as a consequence of inertial forces that emerge during the motion. These displacements and rotations can represent a significant source of energy dissipation within the soil–structure system. In practice, inertial interaction induces two distinct effects: (a) it leads to a period elongation because of the deformable soil underneath, and (b) it alters the damping characteristics of the structure, primarily due to the contributions from the hysteresis damping of the surrounding soil and radiation of energy in the form of stress waves transmitted from the foundation to the soil half-space, known as radiation damping. Similarly, comparing time $t = 1.20$ and 1.60 s shows how the foundation barely deforms, averaging the velocity at the interface due to the so-called kinematic interaction. Kinematic interaction arises due to the presence of rigid foundation elements within or on the soil, causing movements at the foundation level to differ from those in the free field. One cause of these deviations is base-slab averaging, which occurs because the stiffness of the foundation system leads to the averaging of ground motion variations within the foundation's footprint, causing deviations from the free-field motions. Another cause of such deviation is embedment effects, which occur as a result of a reduction in foundation-level motions due to the attenuation of ground motion

as depth increases beneath the free surface. This demonstrates that the coupled DRM–PML system can adequately reproduce the half-space conditions and SSI effects.

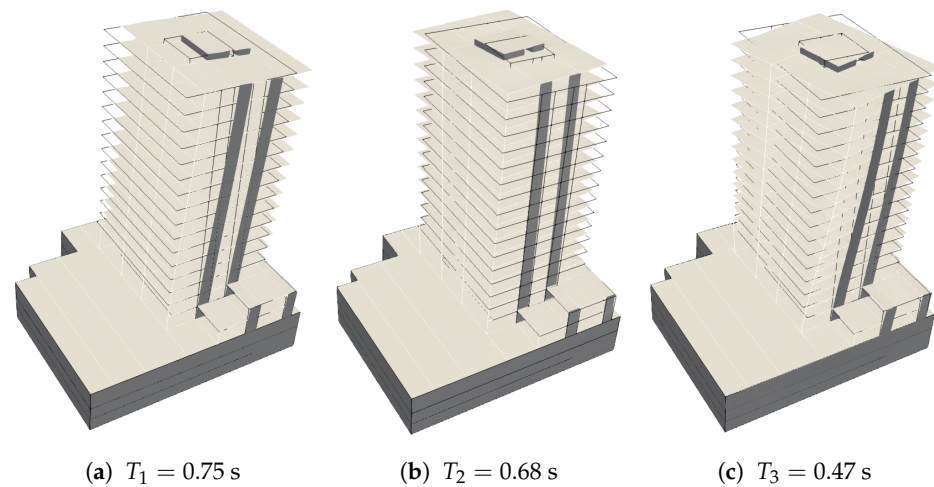


Figure 12. Fixed-base modal shape for the first three modes. The first mode exhibits pure translational behavior, while the second and third modes display rotational behavior. The 3D visualization depicts the deformed configuration in solid white (slabs) and grey (walls) colors, whereas black lines represent the undeformed configuration.

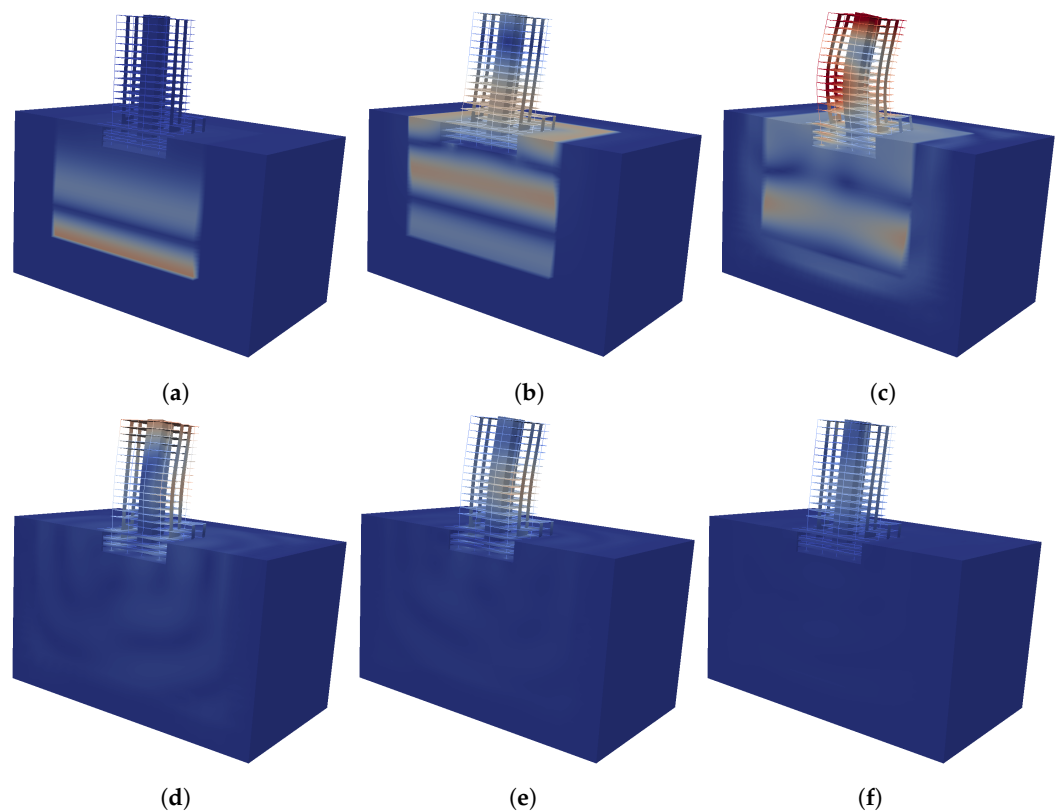


Figure 13. Velocity field amplitude and deformed configuration at time (a) $t = 1.20$ s, (b) $t = 1.60$ s, (c) $t = 2.32$ s, (d) $t = 3.52$ s, (e) $t = 5.20$ s, and (f) $t = 8.00$ s for the problem. The blue color represents a velocity amplitude of 0.0 m/s, while the red color represents a velocity amplitude of 0.2 m/s.

3.1. SSI Effects on Site Response

It is of interest to study the influence of the vibration of the building over the surrounding areas. In order to evaluate the radiated wavefields generated by the building, the perturbed displacement field is calculated as

$$\mathbf{u}_p(\mathbf{x}, t) = \mathbf{u}_{SSI}(\mathbf{x}, t) - \mathbf{u}_{FFM}(\mathbf{x}, t), \tag{17}$$

where $\mathbf{u}_p(\mathbf{x}, t), \mathbf{u}_{SSI}(\mathbf{x}, t), \mathbf{u}_{FFM}(\mathbf{x}, t) : \mathbb{R}^3 \times \mathbb{R}^+ \rightarrow \mathbb{R}^3$ are the perturbation displacement field, the displacement field due to the presence of the building, and the displacement field at the far field (or motion on the soil surface in absence of the building), respectively. These fields are evaluated at coordinate $\mathbf{x} \in \mathbb{R}^3$ on the soil surface at time $t \in \mathbb{R}^+$. The perturbed velocity field $\mathbf{v}_p(\mathbf{x}, t)$ as well as the perturbed acceleration field $\mathbf{a}_p(\mathbf{x}, t)$ can be obtained in a similar manner, as in Equation (17).

The SSI effects on site response are thus defined in the following manner:

- (a) The peak ground displacement ($\mathcal{PGD} : \mathbb{R}^3 \rightarrow \mathbb{R}^+$) of the perturbed displacement field,

$$\mathcal{PGD}(\mathbf{x}) = \max_{t \in [0, T_s]} \|\mathbf{u}_p(\mathbf{x}, t)\|_2, \tag{18}$$

where T_s the simulation time, and $\|\cdot\|_2 : \mathbb{R} \rightarrow \mathbb{R}^+$ is the Euclidean or ℓ^2 vector norm.

- (b) The pseudo-spectral acceleration ($\mathcal{PSA} : \mathbb{R}^3 \times \mathbb{R}^+ \rightarrow \mathbb{R}^+$) of the perturbed acceleration field,

$$\mathcal{PSA}(\mathbf{x}, \omega) = \omega^2 \max_{t \in [0, T_s]} |\mathbf{u}_{sdof}(\mathbf{x}, t)|, \tag{19}$$

where $\mathbf{u}_{sdof}(\mathbf{x}, t)$ is the displacement response evaluated at $\mathbf{x} \in \mathbb{R}^3$ on the soil surface for a single-degree-of-freedom system when $\mathbf{a}_p(\mathbf{x}, t)$ is employed as the input, ω is the angular frequency of a single-degree-of-freedom system, and $|\cdot| : \mathbb{R} \rightarrow \mathbb{R}^+$ is the absolute value function.

Figure 14 shows the \mathcal{PGD} distribution on the soil surface generated by the vibration of the building for different angles of incidence. This figure shows traces of two important SSI phenomena. First, an outward-propagating wavefield is qualitatively similar regardless of incident angle. Second, significant perturbations are generated in the sharp corners of the foundation layout. In particular, a maximum \mathcal{PGD} of 4.5 mm is reached when $\alpha = 30^\circ$, while a minimum \mathcal{PGD} of 0.8 mm is reached when $\alpha = 90^\circ$. Overall, a minimum displacement wavefield of magnitude 1 mm is developed by the building in the surrounding areas. In essence, the soil compliance allows the rocking of the building to generate outgoing waves, as if the vibration building was a source force acting on a half-space. The geometrical complexity of the foundation gives rise to a complex pattern of outgoing waves that may affect other structures near the building, and that can be captured and scrutinized using our 3D FE model.

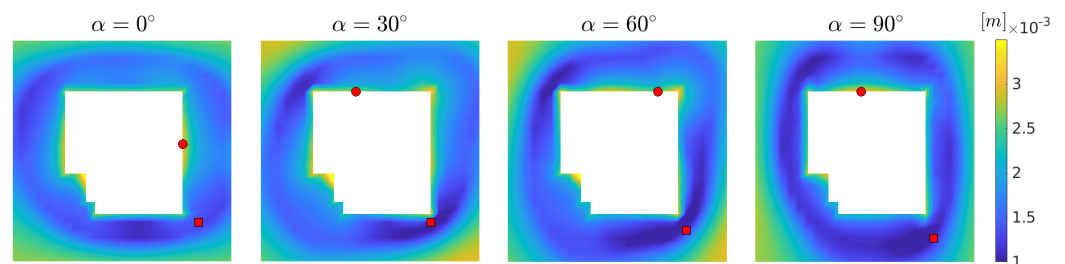


Figure 14. The peak ground displacement (\mathcal{PGD}) distribution on the soil surface generated by the vibration of the building for different angles of incidence. The red solid circle and red solid square represent the location where the maximum and minimum \mathcal{PSA} are attained.

In a similar fashion, Figure 15 shows the pseudo-spectral acceleration (\mathcal{PSA}) for different angles of incidence. This output corresponds to the maximum basal shear experienced by an SDOF system whose fundamental mode has a certain period [102]. In this figure, the grey lines represent the \mathcal{PSA} for all points on the soil surface; the black line is the average of all cases; and the red and blue lines correspond to the maximum and minimum \mathcal{PSA} , respectively, whose locations are displayed in Figure 14 as a red solid circle and square, respectively. Maxima of $\mathcal{PSA} = 5.6 \text{ m/s}^2$ when $\alpha = 0^\circ$, $\mathcal{PSA} = 4.5 \text{ m/s}^2$ when $\alpha = 30^\circ$, $\mathcal{PSA} = 6.3 \text{ m/s}^2$ when $\alpha = 60^\circ$, and $\mathcal{PSA} = 7.3 \text{ m/s}^2$ when $\alpha = 90^\circ$ are obtained. Note that the vibration of the building triggers amplification in hypothetical SDOF between 0.20–0.40 s, which suggests that most of the frequency content of the soil deformation induced by the scattered wavefield stays in that range. It is worth mentioning that this range contains periods substantially shorter than that of the building (the fixed-base period of the building was computed to be 0.75 s using modal analysis, so one would expect the elongated period due to SSI effects to be larger). The prior numbers can be interpreted in terms of geometrical considerations: the shape of the foundation defines the perturbation introduced to the soil at each portion of the interface between the two, the superposition of the different contributions at one point rendering the unique deformation time history of each ground surface location and, by extension, a unique spectrum. Such a spectrum describes a supplementary potential base shake to be felt by surrounding structures. Thus, the simulation allows one to conclude that the building–soil deformation can induce vibrations that may affect structures with very different typologies when compared to the building acting as a source: the level of amplification due to SSI can increase in seismic demand on secondary structures in surrounding areas. In particular, structures such as footbridges, low-rise structures, or social events areas could be potentially affected.

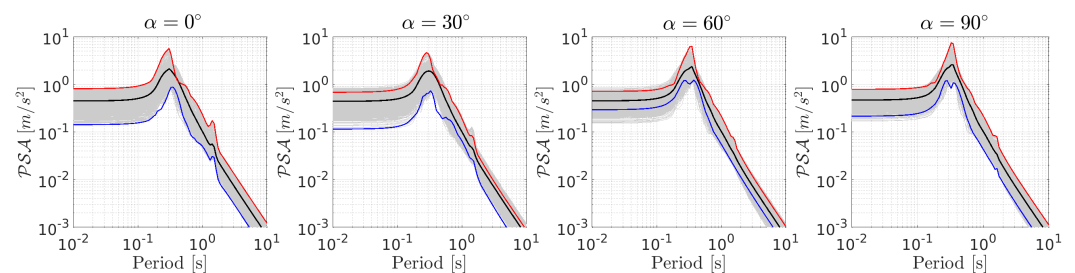


Figure 15. The pseudo-spectral acceleration (\mathcal{PSA}) generated by the vibration of the building for different angles of incidence. The grey lines represent the \mathcal{PSA} for all points on the soil surface, the black line represents its average, and the red and blue lines are the maximum and minimum \mathcal{PSA} .

Finally, Figure 16 shows the vertical component for the perturbed velocity field $\mathbf{v}_p(\mathbf{x}, t)$ considering different angles of incidence. In this figure, the maximum vertical response magnitude is attained at $t^* = 1.20 \text{ s}$ for the four angles. In particular, a maximum value of $\mathbf{v}_p^z(\mathbf{x}, t^*) = -0.063$ and 0.050 m/s at the southwest (square marker) and east (circle marker) foundation sectors when $\alpha = 0^\circ$, a maximum value of $\mathbf{v}_p^z(\mathbf{x}, t^*) = -0.075$ and 0.046 m/s at the southwest and east foundation sectors when $\alpha = 30^\circ$, a maximum value of $\mathbf{v}_p^z(\mathbf{x}, t^*) = -0.068$ and 0.046 m/s at the southwest and north foundation sectors when $\alpha = 60^\circ$, and a maximum value of $\mathbf{v}_p^z(\mathbf{x}, t^*) = -0.042$ and 0.051 m/s at the southwest and north foundation sectors when $\alpha = 90^\circ$, are obtained. Note that, once again, these maximum values are attained at these places as a consequence of the perfect bonding between the foundation and the soil that is imposed through kinematic constraints.

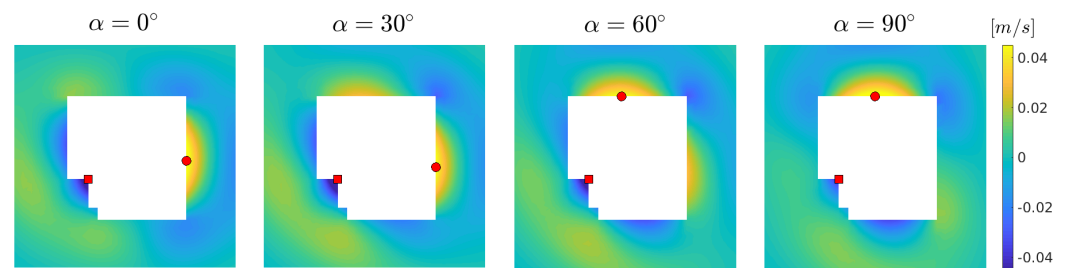


Figure 16. The vertical velocity component for the perturbed velocity field $v_p(\mathbf{x}, t)$ generated by the vibration of the building for different angles of incidence. The positions where the maximum positive and negative velocity magnitudes occur are indicated with a red solid circle and square, respectively.

3.2. SSI Effects on Structural Response

Let $\mathbf{x} \in \mathbb{R}^3$ be the coordinate of the center of the rigid diaphragm, H be the inter-storey height, T_s be the simulation time, and $|\cdot| : \mathbb{R} \rightarrow \mathbb{R}^+$ be the absolute value function. Then, the following structural response quantities can be defined.

- (a) The maximum inter-storey drift ratio ($ISD : \mathbb{R}^3 \rightarrow \mathbb{R}^+$) along a certain direction at i -th storey:

$$ISD(\mathbf{x}) = \frac{1}{H} \max_{t \in [0, T_s]} |\mathbf{u}_i(\mathbf{x}, t) - \mathbf{u}_{i-1}(\mathbf{x}, t)|, \tag{20}$$

where $\mathbf{u}_i(\mathbf{x}, t)$ is the displacement component along the said direction at the diaphragm center of the i -th floor.

- (b) The maximum inter-storey rotation ($ISR : \mathbb{R}^3 \rightarrow \mathbb{R}^+$) at the i -th storey:

$$ISR(\mathbf{x}) = \frac{1}{H} \max_{t \in [0, T_s]} |\theta_i(\mathbf{x}, t) - \theta_{i-1}(\mathbf{x}, t)|, \tag{21}$$

where $\theta_i(\mathbf{x}, t)$ is the rotation along the z -axis of the diaphragm.

- (c) The maximum relative storey acceleration ($MSA : \mathbb{R}^3 \rightarrow \mathbb{R}^+$) at the i -th storey:

$$MSA(\mathbf{x}) = \max_{t \in [0, T_s]} |\mathbf{a}_i(\mathbf{x}, t) - \mathbf{a}_g(\mathbf{x}, t)|, \tag{22}$$

where $\mathbf{a}_i(\mathbf{x}, t)$ is the acceleration response evaluated at the center of the rigid diaphragm, and $\mathbf{a}_g(\mathbf{x}, t)$ is the acceleration evaluated at the ground level.

Figure 17 shows how the drift changes as the angle of incidence of the impinging wave increases. See how when $\alpha = 0$ degrees (the shake is aligned with the x -direction), the maximum drift occurs along the same direction, and, likewise, a similar result happens for $\alpha = 90$ degrees and the y -direction. In these two limit scenarios, the drift is concentrated along one of the two orthogonal directions, which in turn can also be identified with the main axes of inertia: the x -direction corresponds to the stiffest direction, while the y -direction corresponds to the least stiff direction. Therefore, it is logical that the maximum drift, among all the possibilities, corresponds to the y -direction when $\alpha = 90$ degrees, as it can be acknowledged immediately by comparing the first and second panels in Figure 17.

The two intermediate cases, $\alpha = 30, 60$ degrees, display drift along both orthogonal directions simultaneously, with magnitudes bounded by those of the two limit cases. It is also worth remarking on how the drift increases from the base to the first floor, then decreases, and then increases again until it almost reaches the top, with a slight decrease at the very top. This behavior belongs to the reinforcement of intermediate floors, which prompts some intermediate floors to move together with less differential deflections among them. The third panel in Figure 17 shows inter-storey rotation, i.e., the differential torsion between consecutive floors, going from bottom to top. It can be observed from this output that the maximum rotations happen in the case of $\alpha = 0$ degrees, and the minimum occur

when $\alpha = 90$ degrees. The building layout explains this behavior: there is a significant stiffness asymmetry due to a concrete reinforcement wall on one of the flanks that produces a misalignment between the center of mass of the structure and its main axis of inertia, which in turn leads to induced torsion as the building bends. However, such asymmetry is not so acute when considering the orthogonal axis. Hence, the induced torsions are much weaker and more uniform when loading along the y -direction, so the ISR remains substantially smaller. The simulations allow us to quantify these numerically in case of seismic events.

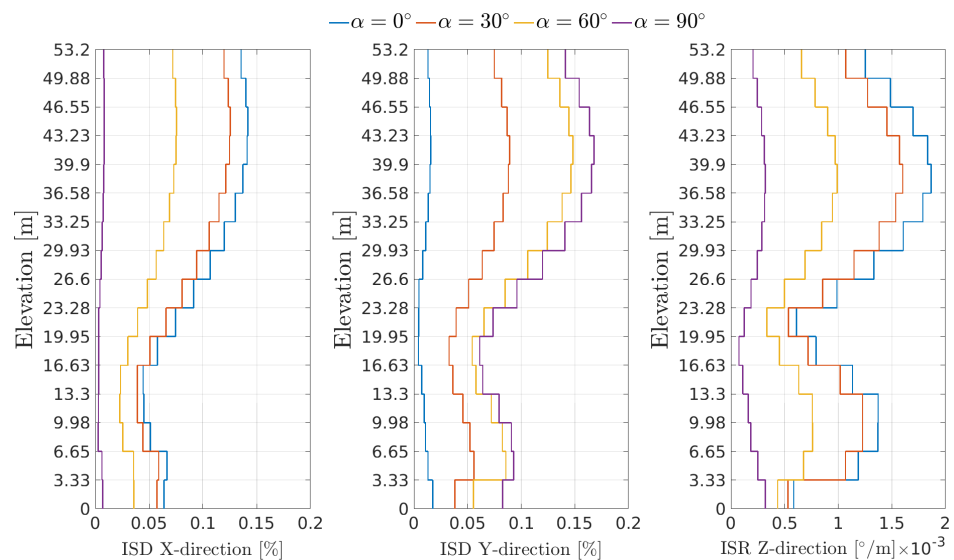


Figure 17. Inter-storey drifts (ISD) along each direction as a function of the angle.

Inter-storey drift and rotation, measuring the differential deformation between consecutive floors, are thus directly correlated with the internal forces that develop within the columns that connect consecutive levels. To account for inertial forces at the different floors, the maximum storey acceleration (with respect to the ground-level acceleration) MSA is introduced. This output indicates the sudden jerk that people and equipment will experience during the seismic event. Therefore, it is an important variable to consider when it comes to utility design and the comfort and safety of occupants (serviceability limit states). The MSA results are represented in Figure 18. Unsurprisingly, the maximum accelerations are experienced at the top floors, and are aligned again with the direction of loading in all four cases. Conversely, it is interesting to note how the stiffening of the intermediate floors also translates into a non-monotonic evolution of the acceleration; this result suggests that the building deforms predominately following a modal shape that is more complex than a simple cantilever beam simplified model.

Lastly, the reader may consider that nonlinear materials and large deformation can also be specified for more accurate analysis in *Seismo-VLAB*. Introducing nonlinear soil behavior opens the door to energy dissipation mechanisms that can reduce building vibrations. However, this can also lead to increased deformation, potentially caused by substantial displacements and rotations developing at the soil–foundation interface. Additionally, introducing geometric nonlinearity into the structural system, primarily driven by significant displacements, may trigger effects such as P-delta, plastic hinges within the beam and column elements, and yield lines within slab elements. The former mechanism introduces an extra source of dissipation within the structural system. Although incorporating a nonlinear analysis may capture a more accurate response, the execution time increases drastically. It is essential to underscore that while these considerations hold significant relevance in structural engineering, their detailed exploration lies outside the scope of this particular example. More technical details regarding this illustrative example can be found in the performance cases H01 provided with the SVL software package.

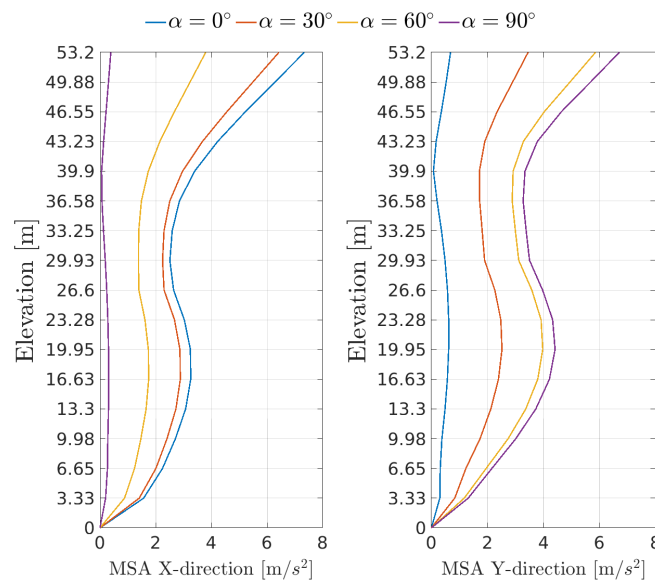


Figure 18. Maximum storey acceleration (*MSA*) along each direction as a function of the angle.

4. Discussion and Conclusions

Seismo-VLAB represents a remarkable advancement in the field of soil–structure interaction (SSI) analysis. Its innovative open-source approach, combining state-of-the-art techniques, advanced parallel computing capabilities, and user-friendly implementation, makes it a pioneering tool for engineers and researchers. By addressing critical limitations in existing software, such as modeling wave propagation in half-spaces and facilitating code customization, SVL empowers users to explore complex SSI scenarios with efficiency and precision. Its versatility and applicability to various SSI problems make it an indispensable resource for the seismic engineering community. SVL not only fills a vital gap, but also propels the field forward, contributing to the analysis for safer and more resilient structures in the face of seismic events.

Building upon its innovative open-source approach and versatile capabilities, *Seismo-VLAB*'s methodology employs state-of-the-art methods for appropriately emulating truncated half-space. A detailed procedure for the validation of DRM and PML for 3D settings is described. The PML implementation includes (1) a recent symmetric hybrid formulation suitable for existing FE codes and (2) a compatible version of DRM for inclined plane incident P, SV, and Rayleigh waves. The DRM and PML implementation is verified using a set of verification cases through problems involving vertical and inclined incident SV waves for inhomogeneous 3D soil. Additionally, a practical application for assessing the SSI effects on the site and structural response for a real 3D building when a vertical SV wave of small amplitude is applied. In particular, the latter application case not only showcases SVL's current modeling and parallel computing capabilities, but also demonstrates its capacity to model real-world earthquake responses in structural engineering.

Furthermore, the coupled DRM–PML technique proves to be a key factor for solving SSI problems. Therefore, the *Seismo-VLAB* project will be disseminated for broader use, since the already-implemented features will allow enthusiastic developers and users to explore other research fields. Some fields where SVL can be useful are (1) the modeling of spatial variability of soil properties for uncertainty quantification in linear and nonlinear models of engineering structures, (2) inverse problems for parameter estimation as well as reliability-based performance analysis in nonlinear finite element models of engineering structures, and (3) site response analysis for the study of amplification or deamplification of seismic waves considering topographic and basin effects. SVL has already proved its suitability to analyze the seismic response of structural systems. The *Seismo-VLAB* project can be downloaded at <https://github.com/SeismoVLAB/SVL> (accessed on 2 May 2023),

and the documentation is available at <http://www.seismovlab.com/> (accessed on 2 May 2023) for more specific details.

Author Contributions: Conceptualization, D.S.K., E.E.S. and D.A.; methodology, D.S.K., E.E.S. and D.A.; software, D.S.K., K.T.N. and E.E.S.; validation, D.S.K., E.E.S., P.A., K.T.N. and J.G.-S.; formal analysis, D.S.K., P.A., K.T.N. and J.G.-S.; investigation, D.S.K., E.E.S. and D.A.; resources, D.A. and A.R.K.; writing—original draft preparation, D.S.K., E.E.S., P.A., K.T.N., J.G.-S., A.R.K. and D.A.; writing—review and editing, D.S.K., E.E.S., P.A., K.T.N., J.G.-S., A.R.K. and D.A.; visualization, D.S.K., K.T.N. and J.G.-S.; supervision, A.R.K. and D.A.; project administration, A.R.K. and D.A.; funding acquisition, A.R.K. and D.A. All authors have read and agreed to the published version of the manuscript.

Funding: This research was possible thanks to the external funding provided by the Pacific Gas and Electric Company (PG&E).

Data Availability Statement: The data presented in this study are available on request from the corresponding author. Examples and verification case used in this manuscript are freely available in the <https://github.com/SeismoVLAB/SVL/03-Validations/02-Performance> (accessed on 2 May 2023) folder.

Acknowledgments: The authors would like to acknowledge the financial support of PG&E that made the development of this code possible.

Conflicts of Interest: The authors declare no conflict of interest. The funders played no part in shaping the study's design, data collection, analysis, or interpretation, nor did they contribute to the manuscript's preparation or the decision to publish the findings.

References

1. Strang, G.; Fix, G.J. *An Analysis of the Finite Element Method*; Prentice-Hall: Englewood Cliffs, NJ, USA, 1973; Volume 212.
2. Quarteroni, A.; Sacco, R.; Saleri, F. *Numerical Mathematics (Texts in Applied Mathematics)*; Springer: Berlin/Heidelberg, Germany, 2006.
3. Bathe, K. *Finite Element Procedures*; Prentice Hall: Upper Saddle River, NJ, USA, 2006.
4. Hughes, T. *The Finite Element Method: Linear Static and Dynamic Finite Element Analysis*; Dover Civil and Mechanical Engineering; Dover Publications: Mineola, NY, USA, 2012.
5. McKenna, F. OpenSees: A Framework for Earthquake Engineering Simulation. *Comput. Sci. Eng.* **2011**, *13*, 58–66. [[CrossRef](#)]
6. Taucer, F.; Spacone, E.; Filippou, F.C. *A Fiber Beam-Column Element for Seismic Response Analysis of Reinforced Concrete Structures*; University of California at Berkeley: Berkeley, CA, USA, 1991.
7. Spacone, E.; Filippou, F.C.; Taucer, F.F. Fibre Beam-Column Model for Non-Linear Analysis of R/C Frames: Part II. Applications. *Earthq. Eng. Struct. Dyn.* **1996**, *25*, 727–742. [[CrossRef](#)]
8. Scott, M.H.; Fenves, G.L. Plastic hinge integration methods for force-based beam-column elements. *J. Struct. Eng.* **2006**, *132*, 244–252. [[CrossRef](#)]
9. Meo, M.; Zumpano, G. On the optimal sensor placement techniques for a bridge structure. *Eng. Struct.* **2005**, *27*, 1488–1497. [[CrossRef](#)]
10. Van der Linden, G.W.; Emami-Naeini, A.; Kosut, R.L.; Sedarat, H.; Lynch, J.P. Optimal sensor placement for health monitoring of civil structures. In Proceedings of the 2011 American Control Conference, San Francisco, CA, USA, 29 June–1 July 2011; pp. 3116–3121. [[CrossRef](#)]
11. Chang, M.; Pakzad, S.N. Optimal Sensor Placement for Modal Identification of Bridge Systems Considering Number of Sensing Nodes. *J. Bridge Eng.* **2014**, *19*, 04014019. [[CrossRef](#)]
12. McCormick, C.W. *MSC/NASTRAN User's Manual*; MSR-39; The MacNeal Schwendler Corporation: Los Angeles, CA, USA, 1981.
13. DeSalvo, G.; Gorman, R.W. *ANSYS Engineering Analysis System User's Manual: For ANSYS Revision 4.4*; Swanson Analysis Systems: Canonsburg, PA, USA, 1989.
14. Hibbitt; Karlsson; Sorensen. *ABAQUS/Standard: User's Manual*; Hibbitt, Karlsson & Sorensen: Pawtucket, RI, USA, 1998; Volume 1.
15. Hallquist, J.O. *LS-DYNA User's Manual*; LS-DYNA, Livermore Software Technology Corporation: Livermore, CA, USA, 1976; Volume 4.
16. *ETABS: Extended Three Analysis of Building System*; Computers and Structures Inc.: Walnut Creek, CA, USA, 2023.
17. *PERFORM3D: Nonlinear Analysis and Performance Assessment for 3D Structures*; Computers and Structures Inc.: Walnut Creek, CA, USA, 2023.
18. *SAP2000: Integrated Software for Structural Analysis and Design*; Computers and Structures Inc.: Walnut Creek, CA, USA, 2023.
19. *FLAC2D/3D: Continuum Modeling for Geomechanics*; Itasca Software: Minneapolis, MN, USA, 2023.

20. Bielak, J.; Christiano, P. On the effective seismic input for non-linear soil-structure interaction systems. *Earthq. Eng. Struct. Dyn.* **1984**, *12*, 107–119. [[CrossRef](#)]
21. Bielak, J.; Loukakis, K.; Hisada, Y.; Yoshimura, C. Domain Reduction Method for Three-Dimensional Earthquake Modeling in Localized Regions, Part I: Theory. *Bull. Seismol. Soc. Am.* **2003**, *93*, 817–824. [[CrossRef](#)]
22. Yoshimura, C.; Bielak, J.; Hisada, Y.; Fernández, A. Domain Reduction Method for Three-Dimensional Earthquake Modeling in Localized Regions, Part II: Verification and Applications. *Bull. Seismol. Soc. Am.* **2003**, *93*, 825–841. [[CrossRef](#)]
23. Basu, U.; Chopra, A.K. Perfectly matched layers for time-harmonic elastodynamics of unbounded domains: Theory and finite-element implementation. *Comput. Methods Appl. Mech. Eng.* **2003**, *192*, 1337–1375. [[CrossRef](#)]
24. Kucukcoban, S.; Kallivokas, L. Mixed perfectly-matched-layers for direct transient analysis in 2D elastic heterogeneous media. *Comput. Methods Appl. Mech. Eng.* **2011**, *200*, 57–76. [[CrossRef](#)]
25. Fathi, A.; Poursartip, B.; Kallivokas, L.F. Time-domain hybrid formulations for wave simulations in three-dimensional PML-truncated heterogeneous media. *Int. J. Numer. Methods Eng.* **2015**, *101*, 165–198. [[CrossRef](#)]
26. MASTODON: Multi-Hazard Analysis for STOchastic Time-DOMain Phenomena; Facility Risk Group at the Idaho National Laboratory: Idaho Falls, ID, USA, 2023.
27. de France, E. Finite Element code *aster*, Analysis of Structures and Thermomechanics for Studies and Research 1989–2017. Available online: www.code-aster.org (accessed on 2 May 2023).
28. Lysmer, J.; Tabatabaie-Raissi, M.; Tajirian, F.; Vahdani, S.; Ostadan, F. *SASSI: A System for Analysis of Soil-Structure Interaction*; University of California: Berkeley, CA, USA, 1981.
29. Jeremić, B.; Jie, G.; Cheng, Z.; Tafazzoli, N.; Tasiopoulou, P.; Pisanó, F.; Abell, J.A.; Watanabe, K.; Feng, Y.; Sinha, S.K.; et al. The Real-ESSI Simulator System. 1988–2020. Available online: <http://real-essi.us/> (accessed on 2 May 2023).
30. McKenna, F.; Fenves, G.L.; Scott, M.H.; Jeremic, B. *Open System for Earthquake Engineering Simulation*; University of California: Berkeley, CA, USA, 2000.
31. Kusanovic, D.S. Improving Reduced Order Models of Soil-Structure Interaction Using an Ensemble Kalman Inversion Finite Element Model Updating Framework. Ph.D. Thesis, The California Institute of Technology, Mechanical and Civil Engineering Department, Pasadena, CA, USA, 2020.
32. Kusanovic, D.S.; Seylabi, E.; Asimaki, D. Seismo-VLAB: An open-source finite element software for seismic meso-scale simulations. *SoftwareX* **2023**, *21*, 101300. [[CrossRef](#)]
33. Guennebaud, G.; Jacob, B.; Niesen, J.; Mierle, K. Eigen v3. 2010. Available online: <http://eigen.tuxfamily.org> (accessed on 2 May 2023).
34. Kucukcoban, S.; Kallivokas, L. A symmetric hybrid formulation for transient wave simulations in PML-truncated heterogeneous media. *Wave Motion* **2013**, *50*, 57–79. [[CrossRef](#)]
35. Karypis, G.; Kumar, V. *METIS—Unstructured Graph Partitioning and Sparse Matrix Ordering System, Version 2.0*; Technical Report; University of Minnesota, Department of Computer Science & Engineering: Minneapolis, MN, USA, 1995.
36. Borja, R.I.; Amies, A.P. Multiaxial Cyclic Plasticity Model for Clays. *J. Geotech. Eng.* **1994**, *120*, 1051–1070. [[CrossRef](#)]
37. Simo, J.; Hughes, T. *Computational Inelasticity*; Springer: New York, NY, USA, 1998; pp. 240–275. [[CrossRef](#)]
38. Borja, R. *Plasticity: Modeling & Computation*; Springer: Berlin/Heidelberg, Germany, 2013.
39. Clarke, L.; Glendinning, I.; Hempel, R. The MPI Message Passing Interface Standard. In *Programming Environments for Massively Parallel Distributed Systems*; Decker, K.M., Rehmann, R.M., Eds.; Monte Verità. Birkhäuser: Basel, Switzerland, 1994; pp. 213–218.
40. Dagum, L.; Menon, R. OpenMP: An Industry-Standard API for Shared-Memory Programming. *IEEE Comput. Sci. Eng.* **1998**, *5*, 46–55. [[CrossRef](#)]
41. Assimaki, D.; Pecker, A.; Popescu, R.; Prevost, J. Effects of spatial variability of soil properties on surface ground motion. *J. Earthq. Eng.* **2003**, *7*, 1–44. [[CrossRef](#)]
42. Popescu, R.; Deodatis, G.; Nobahar, A. Effects of random heterogeneity of soil properties on bearing capacity. *Probabilistic Eng. Mech.* **2005**, *20*, 324–341. [[CrossRef](#)]
43. Stefanou, G. The stochastic finite element method: Past, present and future. *Comput. Methods Appl. Mech. Eng.* **2009**, *198*, 1031–1051. [[CrossRef](#)]
44. El Haber, E.; Cornou, C.; Jongmans, D.; Youssef Abdelmassih, D.; Lopez-Caballero, F.; AL-Bittar, T. Influence of 2D heterogeneous elastic soil properties on surface ground motion spatial variability. *Soil Dyn. Earthq. Eng.* **2019**, *123*, 75–90. [[CrossRef](#)]
45. Pieczyńska-Kozłowska, J.; Bagińska, I.; Kawa, M. The Identification of the Uncertainty in Soil Strength Parameters Based on CPTu Measurements and Random Fields. *Sensors* **2021**, *21*, 5393. [[CrossRef](#)]
46. Savvides, A.A.; Papadarakakis, M. Uncertainty Quantification of Failure of Shallow Foundation on Clayey Soils with a Modified Cam-Clay Yield Criterion and Stochastic FEM. *Geotechnics* **2022**, *2*, 348–384. [[CrossRef](#)]
47. Jensen, H.; Valdebenito, M.; Schuëller, G.; Kusanovic, D. Reliability-based optimization of stochastic systems using line search. *Comput. Methods Appl. Mech. Eng.* **2009**, *198*, 3915–3924. [[CrossRef](#)]
48. Jensen, H.A.; Kusanovic, D.S.; Valdebenito, M.A.; Schuëller, G.I. Reliability-Based Design Optimization of Uncertain Stochastic Systems: Gradient-Based Scheme. *J. Eng. Mech.* **2012**, *138*, 60–70. [[CrossRef](#)]
49. Jensen, H.; Kusanovic, D. On the effect of near-field excitations on the reliability-based performance and design of base-isolated structures. *Probab. Eng. Mech.* **2014**, *36*, 28–44. [[CrossRef](#)]

50. Jensen, H.; Millas, E.; Kusanovic, D.; Papadimitriou, C. Model-reduction techniques for Bayesian finite element model updating using dynamic response data. *Comput. Methods Appl. Mech. Eng.* **2014**, *279*, 301–324. [[CrossRef](#)]
51. Astroza, R. Vibration-Based Health Monitoring and Mechanics-Based Nonlinear Finite Element Model Updating of Civil Structures. Ph.D. Thesis, University of California San Diego, Department of Civil and Environmental Engineering, San Diego, CA, USA, 2015.
52. Ebrahimian, H. Nonlinear Finite Element Model Updating for Nonlinear System and Damage Identification of Civil Structures. Ph.D. Thesis, University of California San Diego, Department of Civil and Environmental Engineering, San Diego, CA, USA, 2015.
53. Kerfriden, P.; Kundu, A.; Claus, S. Adaptivity in Bayesian Inverse Finite Element Problems: Learning and Simultaneous Control of Discretisation and Sampling Errors. *Materials* **2019**, *12*, 642. [[CrossRef](#)]
54. Mohammadi, K. Geometry and Stratigraphy Parameterization of Topography Effects: From the Infinite Wedge to 3D Convex Features. Ph.D. Thesis, The Georgia Institute of Technology, Georgia Tech Library, Atlanta, GA, USA, 2015.
55. Poursartip, B. Topographic Amplification of Seismic Motion. Ph.D. Thesis, University of Texas at Austin, Austin, TX, USA, 2017.
56. Mohammadi, K.; Asimaki, D. Topography Effects Are Not Dominated by Ground Surface Geometry: A Site Effects Paradox. In *Geotechnical Frontiers 2017*; ASCE Library: Lawrence, KS, USA, 2017; pp. 171–181. [[CrossRef](#)]
57. Asimaki, D.; Mohammadi, K. On the complexity of seismic waves trapped in irregular topographies. *Soil Dyn. Earthq. Eng.* **2018**, *114*, 424–437. [[CrossRef](#)]
58. Ayoubi, P.; Asimaki, D.; Mohammadi, K. Basin Effects in Strong Ground Motion: A Case Study from the 2015 Gorkha, Nepal, Earthquake. In *Geotechnical Earthquake Engineering and Soil Dynamics V*; ASCE Library: Lawrence, KS, USA, 2018; pp. 288–296. [[CrossRef](#)]
59. Asimaki, D.; Mohammadi, K.; Ayoubi, P.; Mayoral, J.M.; Montalva, G. Investigating the spatial variability of ground motions during the 2017 Mw 7.1 Puebla-Mexico City earthquake via idealized simulations of basin effects. *Soil Dyn. Earthq. Eng.* **2020**, *132*, 106073. [[CrossRef](#)]
60. Ayoubi, P.; Mohammadi, K.; Asimaki, D. A systematic analysis of basin effects on surface ground motion. *Soil Dyn. Earthq. Eng.* **2021**, *141*, 106490. [[CrossRef](#)]
61. Nguyen, V.Q.; Aaqib, M.; Nguyen, D.D.; Luat, N.V.; Park, D. A Site-Specific Response Analysis: A Case Study in Hanoi, Vietnam. *Appl. Sci.* **2020**, *10*, 3972. [[CrossRef](#)]
62. Hu, Y.; Khatiwada, P.; Tsang, H.H.; Menegon, S. Site-Specific Response Spectra and Accelerograms on Bedrock and Soil Surface. *CivilEng* **2023**, *4*, 311–332. [[CrossRef](#)]
63. Li, J.; Chen, M.; Li, Z. Improved soil–Structure interaction model considering time-lag effect. *Comput. Geotech.* **2022**, *148*, 104835. [[CrossRef](#)]
64. Wu, M.; Ba, Z.; Liang, J. A procedure for 3D simulation of seismic wave propagation considering source-path-site effects: Theory, verification and application. *Earthq. Eng. Struct. Dyn.* **2022**, *51*, 2925–2955. [[CrossRef](#)]
65. Wang, W.; Li, D.Q.; Tang, X.S.; Du, W. Seismic fragility and demand hazard analyses for earth slopes incorporating soil property variability. *Soil Dyn. Earthq. Eng.* **2023**, *173*, 108088. [[CrossRef](#)]
66. Li, J.; Liu, Y.; Lin, G. Implementation of a coupled FEM-SBFEM for soil-structure interaction analysis of large-scale 3D base-isolated nuclear structures. *Comput. Geotech.* **2023**, *162*, 105669. [[CrossRef](#)]
67. Naserkhaki, S.; Aziz, F.N.A.A.; Pourmohammad, H. Earthquake induced pounding between adjacent buildings considering soil-structure interaction. *Earthq. Eng. Eng. Vib.* **2012**, *11*, 343–358. [[CrossRef](#)]
68. Kusanovic, D.S.; Seylabi, E.; Asimaki, D. Optimization of frequency domain impedances for time-domain response analyses of building structures with rigid shallow foundations. *Earthq. Spectra* **2021**, *37*, 1955–1979. [[CrossRef](#)]
69. Nguyen, K.T.; Kusanovic, D.S.; Asimaki, D. Three-dimensional nonlinear soil–Structure interaction for Rayleigh wave incidence in layered soils. *Earthq. Eng. Struct. Dyn.* **2022**, *51*, 2752–2770. [[CrossRef](#)]
70. Nguyen, K.T.; Kusanovic, D.S.; Asimaki, D. Dynamic soil impedance functions for cylindrical structures buried in elastic half-space. *Soil Dyn. Earthq. Eng.* **2022**, *162*, 107431. [[CrossRef](#)]
71. Donnellan, A.; Garcia-Suarez, J.; McPhillips, D.; Asimaki, D.; Goulet, C.; Meng, X.; Devine, S.; Lyzenga, G. Toppling of a Trona Pinnacles Spire following the Mw 5.5 Ridgecrest Aftershock of June 2020. *Seismol. Res. Lett.* **2022**, *93*, 1768–1776. [[CrossRef](#)]
72. Kusanovic, D.S.; Taborda, R.; Asimaki, D. Soil–Structure Interaction Effects on a Regional Scale through Ground-Motion Simulations and Reduced Order Models: A Case Study from the 2008 Mw 5.4 Chino Hills Mainshock. *Bull. Seismol. Soc. Am.* **2023**. [[CrossRef](#)]
73. Crisfield, M.A. *Non-Linear Finite Element Analysis of Solids and Structures: Essentials*; John Wiley & Sons, Inc.: Hoboken, NJ, USA, 1991.
74. Tadmor, E.B.; Miller, R.E.; Elliott, R.S. *Continuum Mechanics and Thermodynamics: From Fundamental Concepts to Governing Equations*; Cambridge University Press: Cambridge, UK, 2011. [[CrossRef](#)]
75. Böhme, D. Characterizing Load and Communication Imbalance in Parallel Applications. Ph.D. Dissertation, RWTH Aachen University, Aachen, Germany, 2014. [[CrossRef](#)]
76. Chevalier, C.; Pellegrini, F. PT-Scotch: A Tool for Efficient Parallel Graph Ordering. *Parallel Comput.* **2008**, *34*, 318–331. [[CrossRef](#)]
77. Devine, K.; Boman, E.; Riesen, L.; Catalyurek, U.; Chevalier, C. Getting Started with Zoltan: A Short Tutorial. In Proceedings of the 2009 Dagstuhl Seminar on Combinatorial Scientific Computing, Istanbul, Turkey, 12–15 March 2009; Sandia National Labs Tech Report SAND2009-0578C.

78. Berge, C. *Graphs and Hypergraphs*; Elsevier Science Ltd.: Amsterdam, The Netherlands, 1985.
79. Karypis, G.; Kumar, V. Multilevel k-Way Hypergraph Partitioning. In Proceedings of the 36th Annual ACM/IEEE Design Automation Conference, DAC '99, New York, NY, USA, 21–25 June 1999; pp. 343–348. [[CrossRef](#)]
80. Gabriel, E.; Fagg, G.E.; Bosilca, G.; Angskun, T.; Dongarra, J.J.; Squyres, J.M.; Sahay, V.; Kambadur, P.; Barrett, B.; Lumsdaine, A.; et al. Open MPI: Goals, Concept, and Design of a Next Generation MPI Implementation. In Proceedings of the 11th European PVM/MPI Users' Group Meeting, Budapest, Hungary, 19–22 September 2004; pp. 97–104.
81. Broquedis, F.; Clet Ortega, J.; Moreaud, S.; Furmento, N.; Goglin, B.; Mercier, G.; Thibault, S.; Namyst, R. hwloc: A Generic Framework for Managing Hardware Affinities in HPC Applications. In Proceedings of the PDP 2010—The 18th Euromicro International Conference on Parallel, Distributed and Network-Based Computing, Pisa, Italy, 17 February 2010.
82. Hursey, J.; Mallove, E.; Squyres, J.M.; Lumsdaine, A. An Extensible Framework for Distributed Testing of MPI Implementations. In Proceedings of the Euro PVM/MPI, Paris, France, 30 September–3 October 2007.
83. Balay, S.; Gropp, W.D.; McInnes, L.C.; Smith, B.F. Efficient Management of Parallelism in Object Oriented Numerical Software Libraries. In *Modern Software Tools in Scientific Computing*; Arge, E., Bruaset, A.M., Langtangen, H.P., Eds.; Birkhäuser Press: Basel, Switzerland, 1997; pp. 163–202.
84. Balay, S.; Abhyankar, S.; Adams, M.F.; Brown, J.; Brune, P.; Buschelman, K.; Dalcin, L.; Dener, A.; Eijkhout, V.; Gropp, W.D.; et al. *PETSc Users Manual*; Technical Report ANL-95/11—Revision 3.12; Argonne National Laboratory: Lemont, IL, USA, 2019.
85. Balay, S.; Abhyankar, S.; Adams, M.F.; Brown, J.; Brune, P.; Buschelman, K.; Dalcin, L.; Dener, A.; Eijkhout, V.; Gropp, W.D.; et al. PETSc Web Page. 2019. Available online: <https://www.mcs.anl.gov/petsc> (accessed on 2 May 2023).
86. Amestoy, P.R.; Duff, I.S.; L'Excellent, J.Y.; Koster, J. A Fully Asynchronous Multifrontal Solver Using Distributed Dynamic Scheduling. *SIAM J. Matrix Anal. Appl.* **2001**, *23*, 15–41. [[CrossRef](#)]
87. Amestoy, P.R.; Guermouche, A.; L'Excellent, J.Y.; Pralet, S. Hybrid scheduling for the parallel solution of linear systems. *Parallel Comput.* **2006**, *32*, 136–156. [[CrossRef](#)]
88. Kawase, H. Time-domain response of a semi-circular canyon for incident SV, P, and Rayleigh waves calculated by the discrete wavenumber boundary element method. *Bull. Seismol. Soc. Am.* **1988**, *78*, 1415–1437. [[CrossRef](#)]
89. Kawase, H.; Aki, K. A study on the response of a soft basin for incident S, P, and Rayleigh waves with special reference to the long duration observed in Mexico City. *Bull. Seismol. Soc. Am.* **1989**, *79*, 1361–1382.
90. Sánchez-Sesma, F.J.; Ramos-Martinez, J.; Campillo, M. An indirect boundary element method applied to simulate the seismic response of alluvial valleys for incident P, S and Rayleigh waves. *Earthq. Eng. Struct. Dyn.* **1993**, *22*, 279–295. [[CrossRef](#)]
91. Sánchez-Sesma, F.J.; Luzon, F. Seismic response of three-dimensional alluvial valleys for incident P, S, and Rayleigh waves. *Bull. Seismol. Soc. Am.* **1995**, *85*, 269–284.
92. Todorovska, M.I. Effects of the wave passage and the embedment depth for in-plane building-soil interaction. *Soil Dyn. Earthq. Eng.* **1993**, *12*, 343–355. [[CrossRef](#)]
93. Zhang, Y.; Yang, Z.; Bielak, J.; Conte, J.; Elgamal, A. Treatment of seismic input and boundary conditions in nonlinear seismic analysis of a bridge ground system. In Proceedings of the 16th ASCE Engineering Mechanics Conference, University of Washington, Seattle, WA, USA, 16–18 July 2003; pp. 16–18.
94. Jeremić, B.; Kunnath, S.; Xiong, F. Influence of soil–foundation–structure interaction on seismic response of the I-880 viaduct. *Eng. Struct.* **2004**, *26*, 391–402. [[CrossRef](#)]
95. Kausel, E.; Roësset, J.M. Stiffness matrices for layered soils. *Bull. Seismol. Soc. Am.* **1981**, *71*, 1743–1761. [[CrossRef](#)]
96. Ancheta, T.D.; Darragh, R.B.; Stewart, J.P.; Seyhan, E.; Silva, W.J.; Chiou, B.S.J.; Wooddell, K.E.; Graves, R.W.; Kottke, A.R.; Boore, D.M.; et al. NGA-West2 Database. *Earthq. Spectra* **2014**, *30*, 989–1005. [[CrossRef](#)]
97. Zhang, W.; Seylabi, E.E.; Taciroglu, E. An ABAQUS toolbox for soil-structure interaction analysis. *Comput. Geotech.* **2019**, *114*, 103143. [[CrossRef](#)]
98. Zhang, W.; Taciroglu, E. 3D time-domain nonlinear analysis of soil-structure systems subjected to obliquely incident SV waves in layered soil media. *Earthq. Eng. Struct. Dyn.* **2021**, *50*, 2156–2173. [[CrossRef](#)]
99. Fathi, A.; Kallivokas, L.F.; Poursartip, B. Full-waveform inversion in three-dimensional PML-truncated elastic media. *Comput. Methods Appl. Mech. Eng.* **2015**, *296*, 39–72. [[CrossRef](#)]
100. Cook, R.D.; Malkus, D.S.; Plesha, M.E.; Witt, R.J. *Concepts and Applications of Finite Element Analysis*; John Wiley & Sons Inc.: Hoboken, NJ, USA, 2007.
101. Jeremić, B.; Jie, G.; Preisig, M.; Tafazzoli, N. Time domain simulation of soil–foundation–structure interaction in non-uniform soils. *Earthq. Eng. Struct. Dyn.* **2009**, *38*, 699–718. [[CrossRef](#)]
102. Clough, R.; Penzien, J. *Dynamics of Structures*; McGraw-Hill: New York, NY, USA, 1994.

Disclaimer/Publisher's Note: The statements, opinions and data contained in all publications are solely those of the individual author(s) and contributor(s) and not of MDPI and/or the editor(s). MDPI and/or the editor(s) disclaim responsibility for any injury to people or property resulting from any ideas, methods, instructions or products referred to in the content.